A Platform for Mitochondrial Profiling in Enriched Kidney Segments Under Thermodynamic Control in Mice and Humans

Stephen T Decker, PhD[1], Precious C Opurum[1,2], Ran Hee Choi, PhD[1,2], Venisia L Paula[1,3,4], Za'rya T Smith[1,4], Anu S Kurian[1], Deborah Stuart[5], Linda Nikolova, PhD[6], Alejandro Sanchez, MD[7,8], Suguru Takayama, MD, PhD[5], Laith Al-Rabadi, MD[5], Nirupama Ramkumar MD, MPH[5], Kelsey H Fisher-Wellman, PhD[9], Katsuhiko Funai, PhD[1,2]

[1]Center for Metabolic Health, University of Utah, Salt Lake City, Utah

[2]Department of Nutrition and Integrative Physiology, University of Utah, Salt Lake City, Utah

[3]Department of Kinesiology, University of Utah, Salt Lake City, Utah

[4]Haumana 'O Pasifika Program, University of Utah, Salt Lake City, Utah

[5]Division of Nephrology and Hypertension, University of Utah School of Medicine, Salt Lake City, Utah

[6]Electron Microscopy Core Facility; University of Utah; Salt Lake City, UT; USA

[7]Division of Urology, Department of Surgery, University of Utah School of Medicine, Salt Lake City, Utah, USA.

[8]Huntsman Cancer Institute, Cancer Hospital, Salt Lake City, Utah, USA.

[9]Department of Cancer Biology, Wake Forest University School of Medicine, Winston-Salem, North Carolina, USA

Corresponding Author: Katsuhiko Funai, kfunai@utah.edu

15 N 2030 E

University of Utah

Salt Lake City, UT 84112

Abstract

Mitochondrial function varies widely across kidney nephron segments, yet conventional approaches lack the resolution and control needed to assess cell-type-specific bioenergetics in situ. We present a methodological platform that enables segment-resolved profiling of mitochondrial respiration, conductance, and membrane potential in freshly isolated mouse and human nephron segments. Combining mechanical sieving and adhesion-based enrichment with permeabilized high-resolution respirometry, we adapted the creatine kinase clamp to quantify oxygen flux and mitochondrial membrane potential across defined free energies. Using this approach, we found that proximal tubules exhibit high respiratory conductance and dynamic mitochondrial polarization, while distal tubules and glomeruli maintain static membrane potential and low conductance. In a model of adenine-induced nephropathy, only proximal tubule mitochondria showed marked reductions in respiration and ATP production. This segment-specific dysfunction was not detectable in bulk mitochondrial isolates. We then demonstrate that these methods can be applied in human kidney samples. Our approach provides thermodynamically anchored, segment-resolved insight into mitochondrial adaptation under physiological and pathological conditions. It is broadly applicable to other tissues with metabolic heterogeneity and compatible with disease models, genetic tools, and pharmacological interventions. This platform bridges a critical gap between conventional respirometry and functional mitochondrial phenotyping in native tissue structures.

Introduction

Kidneys are the second-most bioenergetically active organ per unit mass, surpassed only by the heart[1-7]. This high metabolic activity is required to support the nephron's critical roles in filtration, reabsorption, and excretion. Each day, the kidneys process approximately 130 liters of glomerular filtrate, reabsorbing nearly 99% of this volume back into circulation and excreting only 1–2 liters as urine[8,9]. This extraordinary resorptive capacity is driven by ATP-dependent transport systems that operate continuously to move ions and solutes against their electrochemical gradients[8,10,11]. Key drivers of this active transport include Na^+/K^+-ATPase[10,12], Ca^{2+}/Mg2+-ATPase[13], and vacuolar H^+-ATPase[14,15], which consume significant amounts of ATP to maintain electrolyte and fluid homeostasis.

Mitochondria are central to meeting these energy demands. As the primary generators of ATP via oxidative phosphorylation, mitochondria are highly dynamic organelles capable of adapting structurally and functionally to the cell's metabolic state[16,17]. In response to energetic demands, mitochondria undergo changes in cristae architecture[18,19], fission and fusion dynamics, and the expression and activity of electron transport chain (ETC) components[20-22]. These adaptations enable fine-tuning of mitochondrial efficiency, capacity, and coupling, supporting tissue-specific metabolic requirements.

Within the nephron, mitochondrial morphology, density, and function vary substantially by segment, reflecting the physiological heterogeneity of renal epithelial cells[7]. Proximal tubules (PT), which are responsible for reabsorbing approximately 65% of the glomerular filtrate[10], exhibit the highest mitochondrial density and possess elaborate cristae networks to support their intense ATP requirements[1,23,24]. In contrast, distal tubules (DT) and glomerular cells (Glom), which are involved in fine-tuning solute handling and maintaining the filtration barrier, respectively, exhibit lower mitochondrial content and simpler ultrastructure[23,24]. These segmental differences have important implications for susceptibility to metabolic stress and injury, with the PT being particularly vulnerable due to its high baseline metabolic rate and limited energy reserve[23-25].

46 Despite the recognized heterogeneity in nephron bioenergetics, most existing approaches
47 to studying mitochondrial function in the kidney rely on mitochondria isolated from whole-kidney
48 homogenates or cultured renal cell lines[1,26,27]. These models lack the resolution to detect
49 segment-specific functional differences and are often poorly suited to capturing mitochondrial
50 responses under physiologically relevant conditions. Whole-kidney mitochondrial isolations, while
51 applicable for bulk assessments[28], blend populations from diverse nephron segments and may
52 selectively bias the mitochondrial population[29,30], thereby diluting or masking localized
53 dysfunction. Meanwhile, cultured cell models often fail to recapitulate in vivo cell polarity, tissue
54 architecture, and the integrated stress responses that define renal physiology[26,27,31]. For example,
55 the proximal tubule is known to be a primary target in toxicological models such as the high-
56 adenine diet (AD), which induces fibrosis and tubular injury[32-34]; however, these effects are often
57 obscured in whole-kidney preparations or incompletely modeled in vitro[35].
58 To overcome these limitations, we developed a comprehensive methodological platform
59 to enrich and interrogate mitochondria from specific nephron segments using a combination of
60 mechanical sieving and adhesion-based separation[36,37]. Here, we apply this approach to evaluate
61 how PT, DT, and Glom mitochondria respond to basal conditions and to nephrotoxic stress
62 induced by an AD in mice, and confirm that these methods can be applied to investigate segment-
63 enriched mitochondrial function in humans. We demonstrate that proximal tubules exhibit high
64 bioenergetic adaptability while distal nephron segments and glomeruli maintain static, tightly
65 polarized mitochondria. This platform enables segment-resolved mitochondrial profiling in
66 complex tissues and offers a generalizable strategy for investigating sub-organ energetics in
67 physiology and disease.
68
69 **Results**
70 **Segment-Resolved Isolation Enables Mitochondrial Analysis in Native Nephron Structures**
71 Standard methods for assessing mitochondrial function generally rely on mitochondria

72 isolated from whole kidney tissue (often cortex-only preparations) or cultured renal cell lines.
73 While these approaches are widely used and beneficial, they lack the sensitivity required to detect
74 subtle, segment-specific mitochondrial changes resulting from in vivo interventions. To address
75 these limitations, we employed a sieving and adhesion-based enrichment method (Figure 1A) to
76 isolate distinct nephron segments – PT, DT, and Glom – from freshly harvested mouse
77 kidneys[36,37]. We then ran a standard SUIT protocol on these samples to determine site-specific
78 mitochondrial respiration at (Figure 1B).

79 In brief, kidneys were harvested, the medulla was carefully removed, and the cortical
80 tissue was finely diced to facilitate enzymatic digestion. Tissue digestion was carried out using
81 collagenase type I, followed by sequential filtration through cell strainers with decreasing mesh
82 sizes (100 μm, 70 μm, and 40 μm). PT segments were selectively retained on the 70 μm mesh,
83 while DT and Glom segments passed through and were subsequently collected on the 40 μm
84 mesh. We leveraged their differential adhesive properties to separate DT from Glom further; DT
85 segments adhered to culture dishes, whereas Glom remained suspended. The isolated DT
86 segments were gently scraped from the dishes, and the suspended Glom were separately
87 collected. Transmission electron microscopy confirmed the preservation of mitochondrial
88 ultrastructure within each fraction, with PT samples displaying densely packed mitochondria with
89 well-defined cristae, while DT and Glom exhibited sparser and morphologically simpler
90 mitochondria (Figure 1C). Segmental enrichment was validated by quantitative PCR for nephron-
91 specific markers: Nphs1 (Glom), Slc5a2 (PT), and Aqp2 (DT) (Figure S1).

92 To evaluate mitochondrial function in these enriched nephron segments, we utilized a
93 standardized substrate-uncoupler-inhibitor titration (SUIT) protocol in permeabilized
94 preparations[38]. This approach allowed comprehensive measurement of mitochondrial respiration
95 using HRR (Oroboros O2K) in conjunction with fluorometric assessments (Fluorolog-QM)[39,40].
96 SUIT protocols systematically evaluate ETC functionality by quantifying oxygen consumption
97 rates (JO_2) as specific substrates are sequentially oxidized through Complexes I to IV (Figure

98 1B)[38,41]. This system has the advantage over other systems that have been previously utilized[42,43],
99 as this system allows for the measurement of JO_2 in nonadherent, intact systems, allows for the
100 rapid diffusion of O_2 via continuous stirring (thereby increasing the diffusion of O_2 in the media
101 and increasing the sensitivity of the O_2 flux measurements), customizable SUIT protocols, and
102 continuous, real-time measurement of O_2[41].

103 Notably, we demonstrated that reliable mitochondrial respiration measurements could be
104 achieved with as little as approximately 9 µg of protein per respirometry chamber, as illustrated
105 in initial pilot experiments combining both kidneys from a single mouse (Figure 1D). We conducted
106 additional studies using a single kidney to assess whether this method could be applied to more
107 limited sample volumes, such as when only one kidney is available due to concurrent tissue
108 requirements for other analyses (e.g., histology, PCR, or mass spectrometry). These experiments
109 confirmed that the assay could be successfully performed using one kidney, albeit with some
110 increased technical variability due to lower tissue yield (Figure 1D).

111

112 **Adenine Diet Selectively Impairs Mitochondrial Function in Proximal Tubules**

113 To test the sensitivity of our platform to physiologically relevant injury, we exposed mice
114 to an AD, a well-established model of tubulointerstitial nephropathy that predominantly targets the
115 proximal tubule[32-34,44,45]. Mice were fed alternating concentrations of 0.15% and 0.25% adenine
116 over a two-week cycle to balance toxicity with survival (Figure 2A). AD-fed mice exhibited
117 significant reductions in body weight, kidney mass, and liver mass compared to controls (Figure
118 2B, S2A-B), consistent with systemic catabolic effects. Histological analysis confirmed extensive
119 cortical fibrosis, including tubular atrophy and interstitial expansion (Figure 3C). Quantitative
120 image analysis using an in-house pipeline developed in Python revealed increases in
121 tubulointerstitial fibrosis and increases in tubular luminal area, indicating widespread tubular
122 damage (Figure S3). However, in agreement with previous literature, there were only modest
123 changes in glomerular corpuscle area, fibrotic area, Bowman's space area, and tuft area (Figure

124 S3), indicating that the adenine diet robustly impacts tubules, but not glomeruli[32-34,44].

125 To establish a functional benchmark, we first isolated mitochondria from whole kidney
126 cortex of chow- and AD-fed mice using conventional differential centrifugation. Consistent with
127 prior reports, AD feeding led to a robust ~75% reduction in JO_2 in isolated mitochondrial
128 preparations (Figure 2D), confirming global mitochondrial impairment. However, this bulk
129 measurement masks cellular heterogeneity. We applied our sieving/adhesion method and
130 performed high-resolution respirometry on permeabilized PT, DT, and Glom segments. We
131 observed a striking ~90% reduction in state III JO_2 in PT, a ~75% reduction in DT, and a non-
132 significant decrease in Glom (Figure 2D-G). These data confirm the segment-specific vulnerability
133 of PT and DT to AD-induced mitochondrial dysfunction and reinforce the relative resistance of
134 glomerular cells to AD-induced injury.

135 To assess the downstream bioenergetic consequences of these respiratory changes, we
136 quantified ATP production using an NADPH-based fluorescence assay[40,46,47]. Interestingly, while
137 isolated mitochondria and DT segments from AD-fed mice retained the ability to generate ATP,
138 PT exhibited a significant and disproportionate reduction in ATP production (Figure 2H-K). This
139 suggests that DT mitochondria may retain sufficient inner membrane potential and proton motive
140 force to sustain ATP synthesis despite compromised oxygen consumption, consistent with other
141 observations[23,24]. In contrast, PT mitochondria are more severely compromised, likely reflecting
142 damage to multiple components of oxidative phosphorylation machinery, leading to both impaired
143 respiration and ATP generation[44,45].

144

145 **CK Clamp Reveals Segment-Specific Differences in Respiratory Conductance**

146 While traditional SUIT protocols quantify mitochondrial respiration, they lack the
147 thermodynamic context to assess efficiency or adaptability under dynamic energetic loads.
148 Specifically, SUIT protocols do not allow for quantifying key bioenergetic variables such as the
149 Gibbs free energy of ATP synthesis (ΔG_{ATP}) or the conductance of electrons through the ETC. As

150 a result, they offer limited mechanistic resolution regarding the efficiency and control of oxidative
151 phosphorylation.

152 To overcome these limitations, we implemented the creatine kinase (CK) clamp[3,47-50], a
153 technique that enables fine control of cellular energy charge through the use of phosphocreatine
154 (PCr) and exogenous CK enzyme. This method emulates dynamic changes in energy demand
155 by systematically titrating PCr while maintaining constant levels of ATP and ADP through the
156 action of CK. This system closely mimics physiological transitions between energetic states—
157 ranging from rest (high PCr, low ADP) to high demand (low PCr, high ADP)—and allows for the
158 calculation of respiratory sensitivity to ATP free energy across this gradient (Figure 3A)[47,49,50]. The
159 CK clamp relies on the reversible reaction catalyzed by CK: PCr + ADP ⇌ Cr + ATP. This
160 equilibrium buffers changes in ADP concentration and creates stable energetic states. As PCr
161 increases, ATP is regenerated more readily, reducing the need for mitochondrial ATP synthesis
162 and thereby decreasing *J*O2 (Figure 3B-C). Because the electrochemical proton gradient drives
163 mitochondrial ATP production, the titration of PCr modulates ΔG_{ATP} in a controlled manner, which
164 reflects the driving force for oxidative phosphorylation. By plotting JO_2 against ΔG_{ATP}, we generate
165 a linear force-flow relationship, the slope of which represents the conductance of the ETC (Figure
166 3D)[47,48].

167 Using this approach, we first assessed the response of mitochondria isolated from whole
168 kidney cortex. These preparations demonstrated robust modulation of JO_2 in response to PCr
169 titration, and the AD induced a marked reduction in both oxygen consumption and conductance,
170 confirming a loss of mitochondrial bioenergetic efficiency (Figure 4A-B). These results aligned
171 well with those from SUIT-based assays and served as a baseline for comparison to enriched
172 nephron segment samples. We next applied the CK clamp to enriched PT, DT, and Glom
173 segments obtained using the sieving and adhesion technique. Among these, only PT showed a
174 consistent and significant reduction in respiration in response to the AD (Figure 4C-H). This
175 observation reinforces the conclusion that PTs are the primary targets of bioenergetic dysfunction

176 in this model of renal injury, while DT and Glom remain comparatively resistant.

177 To further interrogate these differences, we quantified the ETC conductance (the slope of
178 the $JO_2/\Delta G_{ATP}$ relationship) and the zero-load JO_2 (y-intercept at $\Delta G_{ATP} \approx 0$). Remarkably, PT
179 mitochondria demonstrated a higher conductance and zero-load JO_2 than both isolated
180 mitochondrial preparations and the other nephron segments under baseline conditions (Figures
181 4I & 4J)[11]. Adenine feeding impaired both metrics across compartments, with the effect clearest
182 in PT (conductance $p = 0.049$; zero-load JO_2 $p = 0.049$), while other segments showed non-
183 significant trends (conductance: $p = 0.182$ mito, $p = 0.472$ DT, $p = 0.425$ glom; zero-load JO_2: p
184 $= 0.112$ mito, $p = 0.441$ DT, $p = 0.402$ glom). Physiologically, higher PT conductance indicates
185 greater responsiveness of electron flux to changes in energetic demand (steeper JO_2 gain per
186 unit decrease in ΔG_{ATP}), and the elevated zero-load JO_2 reflects a larger "no-load" respiratory
187 capacity. The adenine-induced drop in both measures suggests a diet-induced combined insult,
188 making PT mitochondria both the most capable and the most vulnerable to adenine-induced
189 bioenergetic losses in this model.

190

191 **Segmental Regulation of Mitochondrial Membrane Potential Reflects Bioenergetic Demand**

192 Recent studies in tissues like skeletal muscle have demonstrated that $\Delta\Psi_{mt}$ is not static,
193 but rather modulates in response to shifts in energetic demand[17-19]. These adaptations are often
194 associated with cristae remodeling and heterogeneous cristae membrane potentials to optimize
195 ATP synthesis under differing physiological states[18,19]. To evaluate whether similar mitochondrial
196 membrane potential dynamics are evident in kidney mitochondria, we employed the CK clamp in
197 combination with tetramethylrhodamine methyl ester (TMRM), a potentiometric dye whose
198 fluorescence increases with $\Delta\Psi_{mt}$[23,24,38,51]. This approach allowed us to assess changes in
199 mitochondrial polarization across a gradient of bioenergetic states, simulating varying workloads
200 by titrating PCr.

201 Surprisingly, both isolated mitochondria and enriched PT samples exhibited a decrease in

202 TMRM fluorescence as energetic demand decreased, indicated by increasing PCr levels under
203 CK clamp conditions (Figures 5A-D). This decline in $\Delta\Psi_{mt}$ under low ADP availability suggests a
204 tight coupling between ATP turnover and mitochondrial polarization in PT, where a drop in cellular
205 energy demand leads to a proportional decrease in the proton motive force. This behavior
206 contrasts sharply with oxidative tissues such as skeletal muscle, where $\Delta\Psi_{mt}$ typically increases
207 during resting conditions to preserve a reserve capacity for rapid ATP production.

208 This divergent behavior may reflect the distinct physiological roles of these tissues.
209 Skeletal muscle is routinely subject to large, acute swings in ATP demand during transitions from
210 rest to exercise, with energetic demands increasing up to 100-fold during maximal exertion[52,53].
211 To accommodate this, skeletal muscle mitochondria maintain an elevated $\Delta\Psi_{mt}$ during rest, likely
212 functioning as an energetic reservoir that can be rapidly mobilized in times of need. This
213 bioenergetic strategy necessitates the preservation of electrochemical potential even during low
214 metabolic activity, ensuring immediate responsiveness to high ATP turnover upon initiation of
215 physical activity.

216 Conversely, renal PT cells experience fluctuations in energy demand that are less extreme
217 but still dynamic[7,10], as they are driven by continual solute reabsorption and transport processes
218 that adjust in response to systemic needs. While more modest than those seen in skeletal muscle,
219 these variations still require a finely tuned and adaptable mitochondrial system. Mitochondria in
220 PT may function more like an energetic "current," dynamically matching ATP production to
221 demand with high efficiency rather than maintaining a stored potential. This tight feedback
222 between energy need tied to continuous solute reabsorption and $\Delta\Psi_{mt}$ likely optimizes oxidative
223 phosphorylation while minimizing wasteful overproduction of reducing equivalents.

224 In contrast, DT and Glom samples demonstrated no appreciable changes in TMRM
225 fluorescence across the PCr titration series (Figures 5E-H), suggesting a relatively static $\Delta\Psi_{mt}$.
226 This observation likely reflects their lower and more stable bioenergetic demands, consistent with
227 their physiological roles in water conservation and filtration barrier maintenance[7,8]. These cell

228 types do not require the same level of rapid energy responsiveness as PT or skeletal muscle, and
229 as such, their mitochondria may favor stability over adaptability. Mitochondria in these segments
230 may operate near maximal capacity even under basal conditions, potentially prioritizing constancy
231 in ATP production and membrane polarization to support prolonged function over acute
232 responsiveness. This static behavior may reflect an evolutionary adaptation to ensure
233 uninterrupted maintenance of essential renal functions, such as osmotic balance and barrier
234 integrity, under a range of metabolic conditions, suggesting a relatively static $\Delta\Psi_{mt}$.

235 Although this mode of regulation may be beneficial for maintaining baseline function, it
236 could also predispose these segments to injury under sustained energetic surplus. In conditions
237 such as obesity or high-salt diets, chronic mitochondrial hyperpolarization and reduced capacity
238 for $\Delta\Psi_{mt}$ adaptation could promote excessive reactive oxygen species (ROS) production, leading
239 to oxidative damage, inflammation, and eventual decline in renal function. These data support a
240 mechanistic framework linking segment-specific mitochondrial behavior to susceptibility in
241 metabolic kidney disease, particularly in distal nephron and glomerular compartments that lack
242 the energetic adaptability observed in PT mitochondria.

243 To formalize these $\Delta\Psi_{mt}$ dynamics, we derived two summary metrics from each CK-clamp
244 titration. First, we derived a mitochondrial coupling coefficient (the slope $d\Delta\Psi_{mt}/d\Delta G_{ATP}$), which
245 reports how strongly membrane polarization tracks changes in phosphorylation demand, and
246 second, the zero-load $\Delta\Psi$mt (the y-intercept at $\Delta G_{ATP} \approx 0$), which estimates the maximal
247 polarization/reserve when the phosphorylation load is minimal (Fig. 5I–J). In chow controls, PT
248 had the largest coupling coefficient and the highest zero-load $\Delta\Psi_{mt}$ among compartments,
249 consistent with a system designed to modulate polarization rapidly as transport energetic
250 workload fluctuates. Adenine feeding selectively blunted both the coupling coefficient and zero-
251 load $\Delta\Psi_{mt}$ ($p = 0.050$ and $p = 0.034$, respectively) in PT, whereas isolated mitochondria, DT, and
252 glomeruli showed no significant changes (coupling $p = 0.240$ mito, $p = 0.676$ DT, $p = 0.326$ glom;
253 zero-load $p = 0.181$ in mito, $p = 0.892$ in DT,$p = 0.280$ glom). Physiologically, a higher coupling

254 coefficient reflects greater gain in chemiosmotic potential energy, while a higher zero-load $\Delta\Psi_{mt}$
255 reflects a larger polarization reserve available when ATP turnover is clamped low. Thus, the
256 adenine-induced reduction in both metrics indicates that PT mitochondria lose both
257 responsiveness and reserve, aligning with the parallel decreases we observe in ETC conductance
258 and zero-load JO_2. Together, these results position PT as the most bioenergetically capable, yet
259 most vulnerable segment to bioenergetic adaptations to external stimuli.

260 Finally, we plotted JO_2 against $\Delta\Psi_{mt}$ across CK-clamp steps for isolated mitochondria and
261 PT (Fig. S1A–D). The resulting fits were shallow and non-significant, indicating that instantaneous
262 respiration is a weak predictor of membrane polarization in this assay. This is consistent with the
263 indirect coupling between mitochondrial oxygen flux and membrane potential, where membrane
264 polarization is buffered by leak, substrate supply, ion cycling, and ANT/ATP-synthase control.
265 Accordingly, $\Delta\Psi_{mt}$ should be measured directly and interpreted relative to energetic load rather
266 than inferred from JO_2 alone. This does not, however, diminish the value of JO_2 as a surrogate of
267 mitochondrial performance, as oxygen consumption remains undeniably central to OXPHOS.
268 Rather, it underscores the need for multidimensional bioenergetic profiling when characterizing
269 mitochondrial function within physiological systems.

270

271 **Application to Human Renal Samples**

272 We next extended the sieving–adhesion workflow to human renal cortex obtained from
273 non-implantable deceased-donor kidneys and non-neoplastic (tumor-adjacent) cortex from
274 nephrectomies for clear cell renal cell carcinoma (ccRCC). For human tissue, we adjusted the
275 fractionation to reflect larger nephron dimensions[54-57]: coarse material was removed on a 200 μm
276 mesh; intact glomeruli were collected on a 150 μm mesh (consistent with reported human
277 glomerular size), proximal tubules at 70 μm, and distal tubules at 40 μm (Figure 6 A-D). Pilot
278 testing indicated the mouse digitonin dose was insufficient to permeabilize human preparations;
279 doubling the digitonin concentration restored respiration without excessive cytochrome c

280 sensitivity, and only preparations meeting our outer-membrane integrity criterion were advanced.

281 Using the standard SUIT protocol (due to limited samples from donors), we recorded clear,
282 substrate-responsive oxygen flux from enriched human PT, DT, and glomerular fractions with the
283 expected pharmacologic signatures (Figure 6 D-F). Across Complex I and Complex I+II
284 conditions, ADP-stimulated JO_2 ranked PT, DT, and Glom, mirroring the mouse phenotype.
285 Absolute rates showed greater between-sample variability, as anticipated for human tissue (due
286 to possible consequences of donor characteristics and ischemic exposure), but the rank order
287 and inhibitor responses were consistent across sources. These results establish the technical
288 feasibility of segment-resolved mitochondrial bioenergetic assessment in human kidney cortex
289 with minimal front-end adjustments (mesh sizing and increased digitonin), providing a practical
290 bridge from mouse to human and a foundation for application in clinical cohorts.

291

292 **Discussion**

293 Here, we present a methodological framework that integrates nephron segment
294 enrichment with thermodynamically anchored assessments of mitochondrial function using
295 complementary methods. This approach enables simultaneous evaluation of respiratory flux,
296 electron conductance, and membrane potential within segment-resolved kidney structures. By
297 combining cellular enrichment with control over energetic demand, this method provides a more
298 comprehensive picture of mitochondrial performance under physiologically relevant conditions
299 than is possible with traditional techniques[3,23,42].

300 Our results demonstrate that proximal tubule mitochondria exhibit a high degree of
301 energetic adaptability, tightly coupling oxygen consumption and membrane potential to ATP
302 demand across a broad energetic spectrum. This dynamic behavior reflects a capacity to match
303 ATP synthesis to the fluctuating needs of solute reabsorption and active transport. In contrast,
304 mitochondria in distal tubules and glomeruli show markedly limited responsiveness to changes in
305 energetic state, favoring bioenergetic stability over flexibility. These intrinsic differences in

306 energetic plasticity are consistent with the differing physiological roles and energy profiles of each
307 nephron segment and may contribute to segment-specific patterns of vulnerability under
308 pathological conditions.

309 This distinction in mitochondrial adaptability has significant implications for our
310 understanding of kidney physiology and disease. The high flux sensitivity and tight coupling
311 observed in the proximal tubule suggest a system finely tuned for metabolic efficiency but
312 potentially vulnerable to sudden or sustained stress. Meanwhile, the bioenergetic rigidity of distal
313 segments and glomeruli may confer resilience under normal physiological conditions but may limit
314 adaptive responses during energetic excess or mitochondrial dysfunction. These insights
315 contribute to a growing mechanistic framework that links regional mitochondrial function with renal
316 pathophysiology, including the progression of metabolic kidney disease, diabetic nephropathy,
317 and salt-sensitive hypertension.

318 More broadly, this integrative platform offers a versatile tool for dissecting cell-type-
319 specific bioenergetic mechanisms in complex tissues. The ability to measure mitochondrial output
320 across a range of controlled ΔG_{ATP} values while maintaining segmental specificity bridges a critical
321 gap between conventional respirometry and organ-level physiological interpretation. In addition
322 to the kidney, this method is readily extensible to other heterogeneous tissues, such as the heart,
323 brain, and liver, where regional mitochondrial differences drive differential responses to stress
324 and disease. Furthermore, this approach is compatible with models of aging, obesity, genetic
325 manipulation, and pharmacologic intervention, making it ideally suited for both discovery research
326 and translational applications.

327 In summary, the combined approaches of the sieving and adhesion method with high-
328 resolution respirometry and fluorometry, coupled with a SUIT- or CK clamp-based approach
329 introduced here, represent a significant methodological advance for renal mitochondrial
330 physiology. It captures the thermodynamic underpinnings of respiratory control within spatially
331 defined cellular populations, offering both depth and precision in the study of mitochondrial

332 biology. By enabling the detection of subtle, cell-type-specific bioenergetic alterations, this
333 platform lays the groundwork for identifying early signatures of dysfunction and advancing the
334 development of mitochondria-targeted therapies.
335
336

Methods

Animals

All animal procedures were conducted in accordance with the guidelines established by the National Institutes of Health and approved by the Institutional Animal Care and Use Committee (IACUC) at the University of Utah. Male C57BL/6J mice (8–12 weeks old; Jackson Laboratory, Bar Harbor, ME) were used in all experiments. Mice were housed in a specific pathogen-free facility maintained under standard temperature and relative humidity under a 12-hour light/dark cycle. Animals had ad libitum access to food and water throughout the study unless otherwise specified.

Male mice were specifically selected based on well-documented sex-dependent differences in kidney disease progression, with males exhibiting accelerated onset and more severe manifestations of renal injury in multiple experimental models, including AD-induced nephropathy[32,34]. This design consideration allowed for a more robust and reproducible assessment of mitochondrial dysfunction in response to pathophysiological stimuli.

All animals were group-housed (2–5 mice per cage) in individually ventilated cages with routine health monitoring and environmental enrichment. Mice were randomly assigned to experimental groups and monitored daily for signs of distress or adverse effects. Euthanasia was performed between 8 and 10 AM (to minimize circadian variability) using an intraperitoneal injection of a ketamine (100 mg/kg) and xylazine (10 mg/kg) mixture, followed by thoracic puncture to ensure complete exsanguination and death, in accordance with AVMA guidelines. All efforts were made to minimize animal discomfort and reduce the total number of animals used through careful experimental design and statistical planning.

Adenine Diet Intervention

For induction of renal injury, mice were fed a high-adenine diet consisting of alternating concentrations of adenine to balance toxicity and survival. Specifically, animals received chow

363 containing 0.15% adenine (w/w) for one week, followed by 0.25% adenine (w/w) for the
364 subsequent week, in a two-week cyclic regimen repeated for the duration of the intervention
365 period. This alternating diet was designed to induce chronic renal stress while minimizing acute
366 toxicity and mortality. Control mice were maintained on standard chow (Teklad Global 18%
367 Protein Rodent Diet, Envigo). All diet formulations were prepared by Envigo and verified for
368 composition.

369 Body weight, food intake, and signs of discomfort or dehydration were monitored regularly
370 throughout the diet protocol. At the experimental endpoint, mice were euthanized and tissues
371 were harvested for downstream analyses, including histology, nephron segment isolation, and
372 mitochondrial function assays.

373

374 **Transmission Electron Microscopy (TEM)**

375 To evaluate mitochondrial ultrastructure, freshly isolated nephron segments were
376 processed for transmission electron microscopy (TEM). Proximal tubule, distal tubule, and
377 glomerular fractions were isolated using the sieving and adhesion method and immediately
378 submerged in fixative solution (1% glutaraldehyde, 2.5% paraformaldehyde, 100 mM cacodylate
379 buffer pH 7.4, 6 mM CaCl2, 4.8% sucrose) and stored at 4°C for 48 hours. Samples were then
380 processed by the Electron Microscopy Core at University of Utah.

381 Samples underwent 3 × 10-minute washes in 100 mM cacodylate buffer (pH 7.4) prior to
382 secondary fixation (2% osmium tetroxide) for 1 hour at room temperature. Osmium tetroxide as a
383 secondary fixative has the advantage of preserving membrane lipids which are not preserved
384 using aldehyde alone. After secondary fixation, samples were subsequently rinsed for 5 minutes
385 in cacodylate buffer and distilled H2O, followed by prestaining with saturated uranyl acetate for 1
386 hour at room temperature. After prestaining, each sample was dehydrated with a graded ethanol
387 series (2 × 15 minutes each: 30%, 50%, 70%, 95%; then 3 × 20 minutes each: 100%) and acetone
388 (3 × 15 minutes) and were infiltrated with EPON epoxy resin (5 hours 30%, overnight 70%, 3 × 2-

389 hour 40 minute 100%, 100% fresh for embed). Samples were then polymerized for 48 hours at
390 60°C. Ultracut was performed using Leica UC 6 ultratome with sections at 70 nm thickness and
391 mounted on 200 mesh copper grids. The grids with the sections were stained for 20 minutes with
392 saturated uranyl acetate and subsequently stained for 10 minutes with lead citrate. Sections were
393 examined using a JEOL 1200EX transmission electron microscope with a Soft Imaging Systems
394 MegaView III CCD camera.
395
396 **Histology and Image Analysis**
397 *Slide Preparation*
398 Kidney samples were fixed in 10% neutral-buffered formaldehyde for 24–48 hours and
399 submitted to the ARUP Research Histology Core Laboratory at the University of Utah. Tissues
400 were embedded in paraffin, sectioned at 4 μm thickness, and stained with Masson's trichrome to
401 assess morphological changes and fibrotic remodeling.
402 *Whole-slide image acquisition*
403 Kidney sections were stained with Masson's Trichrome (collagen, blue; cytoplasm/muscle,
404 red; nuclei, dark purple). Slides were scanned on a Zeiss AxioScan (ZEISS, Oberkochen,
405 Germany) and converted to pyramidal TIFFs using Fiji. Objective magnification and pixel size
406 were read from image metadata and used to convert pixel counts to physical units (μm and μm^2).
407 All downstream analyses operated on 5X-resolution images.
408 *Automated Segmentation*
409 In Google Colab (Python 3.10), WSIs were optionally harmonized by blended Reinhard
410 normalization ($\alpha = 0.2$) and tiled into 1024×1024 px with 256-px overlap. A MONAI 2D U-Net (3
411 input channels, 7 output classes) was trained on tile/mask pairs to segment glomeruli, tubules,
412 vessels, and background. Slide-level inference used softmax blending with a Hann window; per-
413 pixel labels were assigned by argmax. Class schema, tiling geometry, package versions, and
414 checkpoint paths were logged for reproducibility.

Quantification of WSIs

Metrics were computed within semantic masks on the normalized RGB. Collagen burden used Ruifrok–Johnston color deconvolution with mild reconditioning to limit cross-talk; the collagen channel was converted to a concentration map and thresholded per slide by a fixed percentile, followed by speckle removal and a single opening. The glomerular tuft and Bowman's space were separated from deconvolved intensities along the capsular ridge, and the tuft collagen fraction was reported independently of the periglomerular signal. Tubules were split into instances by a lumen-aware watershed seeded from high-blue (C3) pixels; obvious outliers were filtered by simple shape criteria. For each instance, we report area and standard region-props, lumen area, and pixel-to-μm^2 conversions from per-slide microns-per-pixel. Outputs consist of per-instance tables (glomeruli, tubules) and lightweight QC overlays; timing and provenance logs accompany each run.

Scripts, training images, and output data are publicly available and accessible on GitHub at https://github.com/stdecker/Trichrome_MONAI_Analysis.

Nephron Segment Isolation via Sieving and Adhesion

Mouse Kidney Specimens and Preparation

Immediately following euthanasia, kidneys were harvested, decapsulated, and placed in ice-cold Hanks' Balanced Salt Solution (HBSS) without calcium and magnesium. The renal medulla was carefully dissected away to enrich for cortical tissue. Cortices were minced using a sterile single-use razor blade into ~1 mm^3 fragments and incubated in 1 mg/mL collagenase type I (Sigma-Aldrich, SCR103) dissolved in HBSS at 37°C for 20 minutes with gentle agitation. The digested suspension was passed sequentially through nylon mesh strainers (100 µm, 70 µm, and 40 µm) to fractionate nephron segments based on size and adhesion properties.

PT were retained on the 70 µm mesh and rinsed into fresh HBSS. The filtrate was subsequently passed through a 40 µm strainer to collect remaining nephron fragments, which

441 were enriched for DT and Glom. This 40 μm fraction was allowed to settle in a 60 mm tissue
442 culture dish for 2 minutes at room temperature. DT adhered to the plastic surface, whereas Glom
443 remained suspended. The Glom-enriched supernatant was gently removed, filtered again through
444 a clean 40 μm mesh, and washed in HBSS. DT were then carefully scraped from the culture dish
445 and resuspended.

446 *Human Kidney Specimens and Preparation*

447 Human renal cortex was obtained under institutional approval from two sources: non-
448 implanted deceased-donor kidneys (declined for transplantation) and non-neoplastic (tumor-
449 adjacent) cortex from nephrectomies for clear cell renal cell carcinoma. Tissue was kept on ice,
450 trimmed to remove capsular fat and medulla, minced, and processed using the same sieving–
451 adhesion workflow as for mouse with human-specific mesh cutoffs: coarse material was removed
452 on a 200 μm screen; glomeruli were collected on 150 μm; proximal tubules (PT) on 70 μm; and
453 distal tubules (DT) on 40 μm.

454 All samples were centrifuged at 1,000 × g for 5 minutes and resuspended in mitochondrial
455 isolation medium (MIM) for subsequent bioenergetic analyses. Aliquots were taken for qPCR-
456 based marker validation and electron microscopy to confirm segmental enrichment and
457 mitochondrial structural preservation.

458

459 **Mitochondrial Isolation**

460 Mitochondria were isolated from whole mouse kidney cortical tissue for respirometric and
461 biochemical analyses[28,46]. All tissues were harvested between 9:00 AM and 11:00 AM to minimize
462 circadian variability. Immediately following euthanasia, kidneys were removed, decapsulated, and
463 the renal cortex was rapidly dissected and placed in ice-cold MIM consisting of 300 mM sucrose,
464 10 mM HEPES, 1 mM EGTA, and 1 mg/mL bovine serum albumin (BSA) (pH 7.4).

465 Tissue samples were minced with sterile scissors and gently homogenized using a Teflon-
466 glass Potter-Elvehjem homogenizer on ice to preserve mitochondrial integrity. The homogenate

467 was first centrifuged at 800 × g for 10 minutes at 4°C to pellet nuclei and cell debris. The resulting
468 supernatant was collected and centrifuged at 1,300 × g for 10 minutes to further clarify the
469 mitochondrial suspension. This supernatant was then centrifuged at 10,000 × g for 10 minutes at
470 4°C to pellet intact mitochondria.

471 The final mitochondrial pellet was resuspended in a minimal volume of fresh MIM buffer
472 depending on the pellet size and experimental application. All mitochondrial preparations were
473 maintained on ice and used immediately for downstream assays, including high-resolution
474 respirometry and ATP production measurements. Protein concentrations were determined using
475 the Pierce BCA Protein Assay Kit (Thermo Fisher Scientific, #23225) following the manufacturer's
476 instructions. All steps were performed at 4°C or on ice to preserve mitochondrial function and
477 minimize proteolytic degradation.

478

479 **Real-time polymerase chain reaction (RT-qPCR)**

480 For gene expression analysis, freshly sieved nephron segments (PT, DT, and Glom) were
481 prepared using the Direct-zol RNA Miniprep Kit (Zymo Research) according to the manufacturer's
482 protocol, including an on-column DNase digestion step. RNA purity and concentration were
483 assessed spectrophotometrically, and 1 µg of total RNA was reverse transcribed using the iScript
484 cDNA Synthesis Kit (Bio-Rad, Hercules, CA).

485 Quantitative PCR (qPCR) was performed using SYBR Green-based detection (Thermo
486 Fisher Scientific) in 384-well plates prepared and run by the University of Utah Genomics Core
487 Facility. Expression of kidney injury and fibrosis-related genesPre-validated primer sequences
488 were obtained from the PrimerBank database or prior publications. Relative mRNA levels were
489 normalized to the ribosomal reference gene RPL32 using the ΔΔCt method. Segmental
490 enrichment was validated using primers for segment-specific markers. Nephrin (Nphs1) was used
491 as a glomerular marker (forward: 5'-GACCAGAGGAAGGCATCAAGC-3'; reverse: 5'-
492 GCACAACCTTTATGCAGAACCAG-3'), Slc5a2 (SGLT2) as a proximal tubule marker (forward:

493 5'-CAGACCTTCGTCATTCTTGCCG-3'; reverse: 5'-GTGCTGGAGATGTTGCCAACAG-3'), and
494 AQP2 as a distal tubule marker (forward: 5'-GCCATCCTCCATGAGATTACCC-3'; reverse: 5'-
495 CGCTCATCAGTGGAGGCAAAGA-3').
496
497 **Mitochondrial Assays**
498 ***Substrate-Inhibitor Titration Protocol***
499 *Isolated Mitochondria*
500 Oxygen consumption by isolated mitochondria was assessed using the Oroboros
501 Oxygraph O2K high-resolution respirometry system (Oroboros Instruments, Innsbruck, Austria),
502 following standard protocols and calibration procedures[28,46]. Mitochondria (75 µg of protein) were
503 resuspended in 2 mL of respiration buffer (Buffer Z) composed of 105 mM MES potassium salt,
504 30 mM potassium chloride (KCl), 10 mM monopotassium phosphate (KH2PO4), 5 mM
505 magnesium chloride (MgCl2), and 0.5 mg/mL bovine serum albumin (BSA), adjusted to pH 7.2.
506 Buffer Z was equilibrated in the oxygraph chambers at 37°C, while stirring at 750 RPM, prior to
507 sample addition. Following baseline stabilization, mitochondrial respiration was sequentially
508 stimulated by the addition of substrates to support Complex I- and II-linked respiration: 0.5 mM
509 malate, 5 mM pyruvate, 5 mM glutamate, 2 mM ADP, 10 mM succinate, and 1.5 µM FCCP
510 (carbonyl cyanide-p-trifluoromethoxyphenylhydrazone). Oxygen consumption was continuously
511 recorded and analyzed using DatLab software.
512 *Enriched Nephron Segments*
513 Mitochondrial oxygen consumption in freshly enriched nephron segments was assessed
514 similarly to isolated mitochondria. Proximal tubules (PT), distal tubules (DT), and glomeruli (Glom)
515 were resuspended in 0.5 mL of Buffer Z (105 mM MES potassium salt, 30 mM KCl, 10 mM
516 KH_2PO_4, 5 mM $MgCl_2$, and 0.5 mg/mL BSA, pH 7.2) stirring at 750 RPM. Permeabilization was
517 achieved using 5 µL for mouse experiments and 10 µL for human experiments of 0.81 mM
518 digitonin (final concentration: 4 µM and 8 µM), followed by sequential substrate additions to probe

519 electron transport chain function under saturating conditions of hyperoxygenation (200-250 μM
520 O_2) adapted for tissue diffusion limitations: 5 μL of 0.2 M malate (2 mM), 2.5 μL of 1 M pyruvate
521 (5 mM), 5 μL of 1 M glutamate (10 mM), 5 μL of 0.5 M ADP (5 mM), 5 μL of 1 mM cytochrome c
522 (10 μM), and 10 μL of 0.5 M succinate (10 mM). Maximal uncoupled respiration was induced
523 stepwise with 2 μL of 0.1 mM FCCP (final concentration: 0.4 μM). Approximately 18.75 μg of
524 protein was used per chamber unless otherwise stated. Oxygen consumption was continuously
525 recorded using DatLab software, and only preparations with intact outer mitochondrial
526 membranes (as assessed by the cytochrome c increase of <20% based on pilot data and other
527 published reports[38,58]) were included in analyses.
528 All measurements were carried out at 37°C to mimic physiological conditions. Care was
529 taken to avoid oxygen limitation, and all chambers were re-oxygenated between runs if needed.
530
531 ***Mitochondrial ATP Production***
532 *Isolated Mitochondria*
533 ATP production was quantified fluorometrically using a Horiba Fluoromax 4 fluorometer
534 (Horiba Scientific, USA) by coupling ATP synthesis to NADPH production through an enzymatic
535 cascade as previously described[46]. Assays were performed in using the same substrate
536 conditions as JO_2 at 37°C followed by the addition of 100 μg of protein to each 1 mL assay. The
537 reaction cocktail contained the following components: 2.7 μL of hexokinase (500 U/mL final: 1
538 U/mL), 3.4 μL of 1 M glucose (final: 2.5 mM), 5.4 μL of 0.05 M AP5A (final: 0.2 mM), 6.8 μL of
539 glucose-6-phosphate dehydrogenase (G6PDH, 500 U/mL final: 2.5 U/mL), and 6.8 μL of 0.5 M
540 $NADP^+$ (final: 2.5 mM). Substrates were added to support mitochondrial oxidative
541 phosphorylation: 0.5 mM malate, 5 mM pyruvate, 5 mM glutamate, and 10 mM succinate.
542 Fluorescence was monitored continuously over time.
543 ATP production was stimulated with sequential additions of ADP to reflect increasing
544 energetic demand, as used previously in our lab (2 μM, 20 μM, and 200 μM). NADPH-linked

545 fluorescence was recorded and used to calculate ATP production rates from the linear portions
546 of the curve.

547 *Enriched Nephron Segments*

548 Measurements were conducted using a Horiba Fluoromax 4 fluorometer. Assays were
549 performed in using the same substrate conditions as JO_2 with Buffer Z and digitonin at 37°C,
550 followed by the addition of 100 µg of protein to each 1 mL assay. The reaction cocktail contained
551 the following components: 2.7 µL of hexokinase (500 U/mL final: 1 U/mL), 3.4 µL of 1 M glucose
552 (final: 2.5 mM), 5.4 µL of 0.05 M AP5A (final: 0.2 mM), 6.8 µL of glucose-6-phosphate
553 dehydrogenase (G6PDH, 500 U/mL final: 2.5 U/mL), and 6.8 µL of 0.5 M $NADP^+$ (final: 2.5 mM).
554 Substrates were added to support mitochondrial oxidative phosphorylation: 10 µL of 0.2 M malate
555 (final: 2 mM), 5 µL of 1 M pyruvate (final: 5 mM), 10 µL of 1 M glutamate (final: 10 mM), and 20
556 µL of 0.5 M succinate (final: 10 mM). Fluorescence was monitored continuously over time.

557 ATP production was stimulated with sequential additions of ADP to reflect increasing
558 energetic demand, following a dosing scheme adapted from skeletal muscle protocols: 50 µL of
559 0.0005 M (final: 0.025 mM), 50 µL of 0.0005 M (final: 0.05 mM), 10 µL of 0.005 M (final: 0.1 mM),
560 30 µL of 0.005 M (final: 0.25 mM), and 9.5 µL of 0.5 M (final: 5 mM). NADPH-linked fluorescence
561 was recorded and used to calculate ATP production rates from the linear portions of the curve.

562

563 ***Creatine Kinase Clamp***

564 *Isolated Mitochondria*

565 The thermodynamic control of mitochondrial respiration in isolated mitochondria was
566 assessed using the creatine kinase (CK) clamp technique under saturating substrate conditions[47].
567 Experiments were performed using high-resolution respirometry in Oroboros O2K instruments
568 (Oroboros Instruments, Innsbruck, Austria) at 37°C in 2 mL Buffer Z.

569 To initiate the CK clamp, 10 µL of 20,000 U/mL creatine kinase (final: 20 U/mL), 2 µL of
570 0.2 M phosphocreatine (final: 0.2 mM), and 10 µL of 0.5 M ATP (final: 5 mM) were added

571 sequentially. Mitochondria (75 µg protein) were added to the chamber and substrates were
572 introduced to support Complex I and II activity: 5 µL of 1 M pyruvate (final: 5 mM), 5 µL of 1 M
573 glutamate (5 mM), 5 µL of 0.2 M malate (1 mM), and 10 µL of 0.5 M succinate (5 mM).

574 Phosphocreatine was titrated in a stepwise fashion to establish progressively reduced
575 energetic demand: 6.5 µL of 0.75 M (5 mM), 12 µL (9 mM), and 6 µL (6 mM). To evaluate ATP
576 synthase-dependent respiration, 1 µL of 0.02 mM oligomycin (final: 0.01 µM) was added.
577 Uncoupled respiration was assessed by stepwise addition of FCCP: 1 µL of 0.5 mM (0.5 µM),
578 followed by 1 µL of 1 mM (1 µM), 2 µL (2 µM), and 1 µL (1 µM). Inhibition of respiration was
579 confirmed by the addition of 1 µL of 0.5 mM antimycin A (final: 0.5 µM).

580 Respiratory flux was recorded continuously using DatLab software and normalized to total
581 protein content.

582 *Nephron Segments*

583 Measurements were performed in Oroboros Oxygraph O2K chambers at 37°C using
584 freshly isolated and permeabilized nephron segments (18.75 µg protein in 0.5 mL Buffer Z) under
585 hyperoxygenation (200-250 µM O2). Tissues were permeabilized digitonin followed by sequential
586 reagent additions to establish a CK-clamped energetic environment. The clamp was initiated by
587 addition of 5 µL of 20,000 U/mL creatine kinase (final: 10 U/mL), 2.5 µL of 0.2 M phosphocreatine
588 (final: 1 mM), and 5 µL of 0.5 M ATP (final: 5 mM). To support oxidative phosphorylation,
589 substrates were added as follows: 5 µL of 0.2 M malate (2 mM), 2.5 µL of 1 M pyruvate (5 mM),
590 5 µL of 1 M glutamate (10 mM), 10 µL of 0.5 M succinate (10 mM), and 5 µL of 1 mM cytochrome
591 c (10 µM).

592 To impose a progressive energetic gradient and simulate declining ATP demand,
593 phosphocreatine was titrated in successive steps: 3.25 µL of 0.75 M (5 mM), 6 µL of 0.75 M (9
594 mM), and 4 µL of 0.75 M (6 mM). This approach allowed dynamic assessment of mitochondrial
595 respiratory sensitivity to ΔG_{ATP}. After stabilization at the lowest energetic demand, 0.5 µL of 0.02
596 mM oligomycin (final: 0.02 µM) was introduced to inhibit ATP synthase and quantify proton leak

597 respiration. Finally, maximal uncoupled respiration was determined by addition of 2 μL of 0.1 mM
598 FCCP (final: 0.4 μM).
599 Oxygen flux was continuously recorded using DatLab software (Oroboros Instruments).
600 Preparations were included only if outer mitochondrial membrane integrity was confirmed by the
601 cytochrome c addition test (<10% stimulation). Respiration rates were normalized to total protein
602 concentration as determined by BCA assay.
603
604 ***Mitochondrial Membrane Potential Assay Using TMRM***
605 Mitochondrial membrane potential (ΔΨmt) inwas assessed using a fluorometric assay
606 based on the potentiometric dye tetramethylrhodamine methyl ester (TMRM)[47,51]. All
607 measurements were performed at 37°C in 1 mL quartz or optical glass cuvettes using a Horiba
608 Fluoromax 4 fluorometer (Horiba Scientific, USA) equipped with magnetic stirring. The assay
609 buffer was Buffer Z supplemented with 5 mM creatine monohydrate (freshly prepared). Each well
610 contained 100 μg of protein and was permeabilized with 5 μL of 1 mg/mL digitonin (isolated
611 mitochondria did not have digitonin).
612 Assay buffer was further supplemented with 0.2 μM TMRM immediately prior to use. A
613 substrate mix was added to support mitochondrial respiration, consisting of 2.5 μL of 1 M pyruvate
614 (5 mM), 2.5 μL of 1 M glutamate (5 mM), 2.5 μL of 0.2 M malate (1 mM), and 10 μL of 0.5 M
615 succinate (10 mM).
616 The CK clamp was initiated with 5 μL of 20,000 U/mL creatine kinase (final: 10 U/mL), 2.5
617 μL of 0.2 M phosphocreatine (1 mM), and 5 μL of 0.5 M ATP (5 mM). Phosphocreatine was titrated
618 in a stepwise fashion to progressively increase energy supply: 3.25 μL of 0.75 M (5 mM), 6 μL (9
619 mM), and 4 μL (6 mM). After establishing steady-state ΔΨmt at each energy state, 1 μL of 0.02
620 mM oligomycin (final: 0.02 μM) was added to inhibit ATP synthase. Maximal depolarization was
621 induced with 2 μL of 0.5 mM FCCP (0.5 μM) and 1 μL of 0.5 mM antimycin A (0.5 μM).
622 To determine the appropriate excitation and emission settings, a preliminary excitation

623 scan was performed from 480 to 585 nm, with emission fixed at 600 nm, under four conditions:
624 (1) buffer only, (2) buffer + mitochondria, (3) buffer + mitochondria + 10 mM succinate, and (4)
625 buffer + mitochondria + 10 mM succinate + 5 μM FCCP. The two excitation wavelengths showing
626 the greatest difference between conditions (3) and (4) were selected for subsequent ratiometric
627 fluorescence measurements. For all assays, optimized excitation/emission settings were 577/552
628 nm.

629 Data were expressed as the ratio of TMRM fluorescence under energized versus
630 depolarized states and normalized to protein content.

631

632 ***Gibbs Free Energy Calculation***

633 The Gibbs free energy of ATP hydrolysis (ΔG_{ATP}) was calculated to quantify the
634 thermodynamic driving force governing mitochondrial energy transduction under CK-clamped
635 conditions[47]. ΔG_{ATP} was derived using the modified Nernst equation:

636 $$\Delta G_{ATP} = \Delta G^{\circ\prime}{}_{ATP} + RT\ln\left(\frac{[ADP][Pi]}{[ATP]}\right)$$

637 where $\Delta G^{\circ\prime}{}_{ATP}$ is the standard free energy change for ATP hydrolysis (typically −30.5
638 kJ/mol), R is the universal gas constant (8.314 $J \cdot mol^{-1} \cdot K^{-1}$), T is the absolute temperature in
639 Kelvin (310 K for 37°C), and [ADP], [Pi], and [ATP] are the molar concentrations of ADP, inorganic
640 phosphate, and ATP, respectively.

641 In the CK clamp system, [ATP] and [ADP] were not directly added in varying
642 concentrations, but instead modulated indirectly via the creatine kinase/phosphocreatine buffer
643 system, according to the equilibrium:

644 $PCr + ADP + H^+ \rightleftharpoons ATP + Cr$

645 Because the CK reaction is near equilibrium under our assay conditions, the
646 concentrations of ATP and ADP can be inferred from known values of total ATP, PCr, and Cr
647 using the equilibrium constant of the reaction ($K'CK \approx 1.66 \times 10^9\ M^{-1}$). The assumption of near-

648 equilibrium enables computation of the [ADP]/[ATP] ratio from the known PCr/Cr ratio at each
649 titration point. ΔG_{ATP} values were then calculated across the PCr titration series to generate a
650 force-flux relationship for each biological replicate. Conductance was defined as the slope of the
651 linear regression of JO_2 versus ΔG_{ATP}.

652 These values provide a thermodynamic framework for interpreting bioenergetic efficiency
653 and mitochondrial responsiveness across different nephron segments and conditions. ΔG_{ATP}
654 values and associated parameters can be easily calculated using the web-based bioenergetic
655 calculator available at: https://dmpio.github.io/bioenergetic-calculators/[47].

656

657 **Data Analysis and Statistics**

658 Mitochondrial respiratory conductance and membrane potential conductance were
659 calculated by linear regression of oxygen consumption or TMRM signal, respectively, against the
660 corresponding ΔG_{ATP} across phosphocreatine titration steps. The slope of this regression line was
661 used as a measure of respiratory or electrochemical conductance.

662 Statistical analyses were performed in R version 4.5.1. Unless stated otherwise, tests
663 were two-sided with α=0.05, and data are reported as mean ± SEM. Longitudinal body mass (Diet
664 × Time) was analyzed by two-way ANOVA with Holm-adjusted post hoc contrasts; terminal body,
665 kidney, and liver mass were compared with unpaired two-tailed Student's t-tests. Histology
666 endpoints were evaluated with linear mixed-effects models (random intercept for individual mice)
667 and estimated marginal means/contrasts via the emmeans package (Holm adjustment).
668 Mitochondrial flux (JO_2, J_{ATP}, CK Clamp) experiments were analyzed using an. Linear trends were
669 fit by ordinary least squares using *lm()* on a per-experiment basis, with mean slopes summarized
670 (e.g., Figures 4 and 5B, D, F, H, I). Model assumptions (normality, homoscedasticity) were
671 evaluated from residuals; when materially violated, variance-stabilizing transformations or the
672 prespecified nonparametric approach were applied. Analyses were conducted using the R
673 packages tidyverse, ggprism, ggbeeswarm, rstatix, ARTool, ggpubr, multcomp, reshape2,

674 ggcompare, mutoss, emmeans, and svglite.

675

676 **Acknowledgments**

677 We gratefully acknowledge the support of the University of Utah Health Sciences Core Facilities.
678 Specifically, we thank the Electron Microscopy Core Facility for assistance with ultrastructural
679 analyses, the Cell Imaging Core Facility for support with fluorescence microscopy, ARUP
680 histological services, and the Genomics Core Facility for quantitative PCR services. Their
681 expertise and resources were instrumental in the completion of this study. Schematics in this
682 manuscript were generated using BioRender.

683

684 **Funding**

685 This work was supported by the following grants from the National Institutes of Health: NIDDK
686 R01-DK107397, NIDDK R01-DK127979, NIGMS R01-GM144613, and NIA R01-AG074535 to
687 Katsuhiko Funai; NIDDK R01-DK133271 to Nirupama Ramkumar; NIDDK R01-DK132487 to
688 Laith Al-Rabadi; NCI R01-CA278826 to Kelsey H. Fisher-Wellman; and Ruth L. Kirschstein
689 National Research Service Award 5T32DK091317 to Stephen Decker. Additional support for S.D.
690 was provided by the National Kidney Foundation of Utah and Idaho.

691

692 **Author Contributions**

693 S.D. and K.F. conceived the project. S.D., P.C.O., R.H.C., V.L.P., Z.T.S., A.S.K., D.S., L.N., and
694 A.S. performed experiments and collected data. S.D. and L.N. analyzed the data. All authors
695 contributed to the study design and data interpretation. S.D. and K.F. wrote the manuscript. All
696 authors revised the manuscript and approved the final version.

697

698 **Conflict of Interest**

699 The authors declare no conflict of interest.

700

References

1. Bhargava P, Schnellmann RG. Mitochondrial energetics in the kidney. *Nature Reviews Nephrology*. Oct 2017;13(10):629-646. doi:10.1038/nrneph.2017.107
2. Hansen FM, Kremer LS, Karayel O, et al. Mitochondrial phosphoproteomes are functionally specialized across tissues. *Life Sci Alliance*. Feb 2024;7(2)doi:10.26508/lsa.202302147
3. McLaughlin KL, Hagen JT, Coalson HS, et al. Novel approach to quantify mitochondrial content and intrinsic bioenergetic efficiency across organs. *Sci Rep*. Oct 19 2020;10(1):17599. doi:10.1038/s41598-020-74718-1
4. Rolfe DF, Brown GC. Cellular energy utilization and molecular origin of standard metabolic rate in mammals. *Physiol Rev*. 1997;77:731-758.
5. Sarver DC, Saqib M, Chen F, Wong GW. Mitochondrial respiration atlas reveals differential changes in mitochondrial function across sex and age. *eLife*. 2024;
6. Verissimo T, de Seigneux S. New evidence of the impact of mitochondria on kidney health and disease. *Nat Rev Nephrol*. Feb 2024;20(2):81-82. doi:10.1038/s41581-023-00803-z
7. Chevalier RL. Bioenergetics: the evolutionary basis of progressive kidney disease. *Physiol Rev*. Oct 1 2023;103(4):2451-2506. doi:10.1152/physrev.00029.2022
8. Eaton DC, Pooler J. *Vander's renal physiology*. Eighth edition. ed. McGraw-Hill Education/Medical; 2013:vii, 204 pages.
9. Guyton AC, Hall JE. Textbook of Medical Physiology. *13th ed*. 2016;2016:330-332.
10. Zhuo JL, Li XC. Proximal nephron. *Compr Physiol*. 2013;3:1079-1123.
11. Layton AT, Vallon V, Edwards A. Modeling oxygen consumption in the proximal tubule. *Am J Physiol Renal Physiol*. 2015;
12. Feraille E, Doucet A. Sodium-potassium-ATPase-dependent sodium transport in the kidney. *Physiol Rev*. 2001;81:345-418.
13. Kumar R, Penniston JT, Borke JL. Ca-2+-Mg-2+-Atpase Calcium Pumps in the Kidney. *News in Physiological Sciences*. Oct 1988;3:219-222.
14. Wagner CA, Finberg KE, Breton S, Marshansky V, Brown D, Geibel JP. Renal vacuolar H^+-ATPase. *Physiol Rev*. 2004;84:1263-1314.
15. Smith AN, Jouret F, Bord S, et al. Vacuolar H+-ATPase d2 subunit: molecular characterization, developmental regulation, and localization to specialized proton pumps in kidney and bone. *J Am Soc Nephrol*. May 2005;16(5):1245-56. doi:10.1681/ASN.2004090761
16. Decker ST, Funai K. Mitochondrial membrane lipids in the regulation of bioenergetic flux. *Cell Metab*. Sep 3 2024;36(9):1963-1978. doi:10.1016/j.cmet.2024.07.024
17. Picard M, Shirihai OS. Mitochondrial signal transduction. *Cell Metab*. Nov 1 2022;34(11):1620-1653. doi:10.1016/j.cmet.2022.10.008
18. Segawa M, Wolf DM, Hultgren NW, et al. Quantification of cristae architecture reveals time-dependent characteristics of individual mitochondria. *Life Sci Alliance*. Jul 2020;3(7)doi:10.26508/lsa.201900620
19. Wolf DM, Segawa M, Kondadi AK, et al. Individual cristae within the same mitochondrion display different membrane potentials and are functionally independent. *EMBO J*. Nov 15 2019;38(22):e101056. doi:10.15252/embj.2018101056
20. Youle RJ, van der Bliek AM. Mitochondrial fission, fusion, and stress. *Science*. 2012;337:1062-1065.
21. Chan DC. Mitochondrial dynamics and disease. *Annu Rev Pathol*. 2020;15:235-259.
22. Cogliati S, Frezza C, Soriano ME, et al. Mitochondrial cristae shape determines respiratory chain supercomplexes assembly and respiratory efficiency. *Cell*. 2013 2013;doi:10.1016/j.cell.2013.08.032

23. Hall AM, Unwin RJ, Parker N, Duchen MR. Multiphoton imaging reveals differences in mitochondrial function between nephron segments. *J Am Soc Nephrol*. Jun 2009;20(6):1293-302. doi:10.1681/ASN.2008070759

24. Hall AM, Rhodes GJ, Sandoval RM, Corridon PR, Molitoris BA. In vivo multiphoton imaging of mitochondrial structure and function during acute kidney injury. *Kidney Int*. Jan 2013;83(1):72-83. doi:10.1038/ki.2012.328

25. Hall AM, Unwin RJ. The not so 'mighty chondrion': emergence of renal diseases due to mitochondrial dysfunction. *Nephron Physiol*. 2007;105(1):p1-10. doi:10.1159/000096860

26. Nowak G, Schnellmann RG. Improved culture conditions stimulate gluconeogenesis in primary cultures of renal proximal tubule cells. *Am J Physiol*. Apr 1995;268(4 Pt 1):C1053-61. doi:10.1152/ajpcell.1995.268.4.C1053

27. Nowak G, Schnellmann RG. L-ascorbic acid regulates growth and metabolism of renal cells: improvements in cell culture. *Am J Physiol*. Dec 1996;271(6 Pt 1):C2072-80. doi:10.1152/ajpcell.1996.271.6.C2072

28. Opurum PC, Decker ST, Stuart D, et al. Six months of physical inactivity is insufficient to cause chronic kidney disease in C57BL/6J mice. *bioRxiv*. Aug 30 2024;doi:10.1101/2024.08.29.610415

29. Picard M, Taivassalo T, Gouspillou G, Hepple RT. Mitochondria: isolation, structure and function. *The Journal of Physiology*. 2011/09/15/ 2011;589(Pt 18):4413-4421. doi:10.1113/jphysiol.2011.212712

30. Picard M, Ritchie D, Wright KJ, et al. Mitochondrial functional impairment with aging is exaggerated in isolated mitochondria compared to permeabilized myofibers. *Aging Cell*. 2010/12// 2010;9(6):1032-1046. doi:10.1111/j.1474-9726.2010.00628.x

31. Weiss KP, Kim GH. Limitations of in-vitro kidney models. *Kidney Res Clin Pract*. 2021;40:168-178.

32. Zhang Y, Yang X. Adenine-induced CKD model. *Int J Mol Sci*. 2024;25:1097.

33. Gonzalez-Rodriguez D, Moreto M, Guma M. Recovery in adenine-induced kidney injury. *Int J Mol Sci*. 2024;25:4562.

34. Yang Q, Su S, Luo N, Cao G. Adenine-induced animal model of chronic kidney disease: current applications and future perspectives. *Ren Fail*. Dec 2024;46(1):2336128. doi:10.1080/0886022X.2024.2336128

35. Pedraza-Chaverri J, Sapeta-Toussaint A, Tapia E. Mitochondrial dysfunction in renal tubulointerstitial disease. *Arch Med Res*. 2022;53:1-17.

36. Wang H, Sheng J, He H, et al. A simple and highly purified method for isolation of glomeruli from the mouse kidney. *Am J Physiol Renal Physiol*. Nov 1 2019;317(5):F1217-F1223. doi:10.1152/ajprenal.00293.2019

37. Rush BM, Small SA, Stolz DB, Tan RJ. An Efficient Sieving Method to Isolate Intact Glomeruli from Adult Rat Kidney. *J Vis Exp*. Nov 1 2018;(141)doi:10.3791/58162

38. Doerrier C, Garcia-Souza LF, Krumschnabel G, Wohlfarter Y, Mészáros AT, Gnaiger E. High-resolution fluorespirometry and oxphos protocols for human cells, permeabilized fibers from small biopsies of muscle, and isolated mitochondria. *Methods in Molecular Biology*. 2018.

39. Heden TD, Johnson JM, Ferrara PJ, et al. Mitochondrial PE potentiates respiratory enzymes to amplify skeletal muscle aerobic capacity. *Science Advances*. 2019/09/11/ 2019;5(9):eaax8352. doi:10.1126/sciadv.aax8352

40. Gouspillou G, Rouland R, Calmettes G, et al. Accurate determination of the oxidative phosphorylation affinity for ADP in isolated mitochondria. *PLoS One*. 2011;6(6):e20709. doi:10.1371/journal.pone.0020709

41. Schmidt CA, Fisher-Wellman KH, Neufer PD. From OCR and ECAR to energy: Perspectives on the design and interpretation of bioenergetics studies. *J Biol Chem*. Oct 2021;297(4):101140. doi:10.1016/j.jbc.2021.101140

42. McCrimmon A, Domondon M, Sultanova RF, Ilatovskaya DV, Stadler K. Comprehensive assessment of mitochondrial respiratory function in freshly isolated nephron segments. *Am J Physiol Renal Physiol*. May 1 2020;318(5):F1237-F1245. doi:10.1152/ajprenal.00031.2020
43. Gerencser AA, Neilson A, Choi SW, et al. Quantitative microplate-based respirometry with correction for oxygen diffusion. *Anal Chem*. Aug 15 2009;81(16):6868-78. doi:10.1021/ac900881z
44. Sun CY, Hsu HH, Wu MS. Adenine overload induces ferroptosis in proximal tubule cells. *Cell Death Dis*. 2022;13:687.
45. Xiao L, Zhou H, Ma L. Dapagliflozin restores mitochondrial function in adenine nephropathy. *Front Pharmacol*. 2023;14:1095487.
46. Ferrara PJ, Lang MJ, Johnson JM, et al. Weight loss increases skeletal muscle mitochondrial energy efficiency in obese mice. *Life Metab*. Apr 2023;2(2)doi:10.1093/lifemeta/load014
47. Fisher-Wellman KH, Davidson MT, Narowski TM, Lin CT, Koves TR, Muoio DM. Mitochondrial Diagnostics: A Multiplexed Assay Platform for Comprehensive Assessment of Mitochondrial Energy Fluxes. *Cell Rep*. Sep 25 2018;24(13):3593-3606 e10. doi:10.1016/j.celrep.2018.08.091
48. Nelson MAM, Fisher-Wellman KH. Mitochondrial Diagnostics: A Discovery-Based Biochemical Platform for Phenotyping Human Peripheral Blood Cell Mitochondria. *Methods Mol Biol*. 2021;2277:371-389. doi:10.1007/978-1-0716-1270-5_23
49. Willis WT, Jackman MR, Messer JI, Kuzmiak-Glancy S, Glancy B. A Simple Hydraulic Analog Model of Oxidative Phosphorylation. *Med Sci Sports Exerc*. Jun 2016;48(6):990-1000. doi:10.1249/MSS.0000000000000884
50. Glancy B, Barstow T, Willis WT. Linear relation between time constant of oxygen uptake kinetics, total creatine, and mitochondrial content in vitro. *Am J Physiol Cell Physiol*. Jan 2008;294(1):C79-87. doi:10.1152/ajpcell.00138.2007
51. Emaus RK, Grunwald R, Lemasters JJ. Rhodamine 123 as a probe of transmembrane potential in isolated rat-liver mitochondria: spectral and metabolic properties. *Biochim Biophys Acta*. Jul 23 1986;850(3):436-48. doi:10.1016/0005-2728(86)90112-x
52. Hargreaves M, Spriet LL. Skeletal muscle energy metabolism during exercise. *Nat Metab*. Sep 2020;2(9):817-828. doi:10.1038/s42255-020-0251-4
53. Hawley JA, Hargreaves M, Joyner MJ, Zierath JR. Integrative biology of exercise. *Cell*. Nov 6 2014;159(4):738-49. doi:10.1016/j.cell.2014.10.029
54. Samuel T, Hoy WE, Douglas-Denton R, Hughson MD, Bertram JF. Applicability of the glomerular size distribution coefficient in assessing human glomerular volume: the Weibel and Gomez method revisited. *J Anat*. May 2007;210(5):578-82. doi:10.1111/j.1469-7580.2007.00715.x
55. Hall TJ, Insana MF, Harrison LA, Cox GG. Ultrasonic measurement of glomerular diameters in normal adult humans. *Ultrasound Med Biol*. 1996;22(8):987-97. doi:10.1016/s0301-5629(96)00142-1
56. Jennette JC, D'Agati VD, Fogo AB, Nickeleit V, Stokes MB. *Heptinstall's pathology of the kidney*. Eighth edition. ed. Wolters Kluwer,; 2024:1 online resource.
57. Koitabashi K, Okamoto K, Arirto M, et al. Micro-sieving: isolation of whole glomeruli from a single renal needle biopsy sample. *Nephron Clin Pract*. 2011;117(3):c225-9. doi:10.1159/000320198
58. Miller B, Hamilton K, Boushel R, et al. Mitochondrial respiration in highly aerobic canines in the non-raced state and after a 1600-km sled dog race. *PLoS One*. 2017;12(4):e0174874. doi:10.1371/journal.pone.0174874

849 **Figure Legends**

850 **Figure 1**. A) Schematic outlining the sieving procedure in kidneys harvested from mice. B)
851 Protocol outline of the substrate-uncoupler-inhibitor titration (SUIT) protocol. Substrates, which
852 activate the electron transport chain, are added sequentially. Pyruvate and glutamate produce
853 $NADH^+$ via the TCA cycle, which is used as a substrate for Complex I (CI), and in the absence of
854 ADP, represents a "leak" state. ADP is then added to the chambers to activate the production of
855 ATP, thus representing a phosphorylation state. Cytochrome C (CytC), an indicator of membrane
856 integrity, and succinate, a substrate for complex II (CII), are then added to assess CI- and CII-
857 dependent respiration. FCCP is added to assess supramaximal ETC activity. C) Electron
858 microscopy images of the sieved tissues, indicating the abundance and morphological differences
859 between proximal tubule, distal tubule, and glomerular mitochondria (marked by "M"). D) Initial
860 pilot experiments showing that mitochondrial respiration can be measured in enriched samples
861 from mice using both harvested kidneys or a single harvested kidney. *P*: Pyruvate; *G*: Glutamate;
862 *M*: Malate; *D*: ADP; *S*: Succinate; *FCCP*: Carbonyl cyanide 4-(trifluoromethoxy)phenylhydrazone

863 **Figure 2.** A) A schematic outlining the adenine diet protocol. B) Body weights over the course of
864 the study, and kidney weights at the time of euthanasia. C) Repeasentative Masson's Trichrome
865 images of the kidneys of chow-fed and adenine-fed mice. D-G) Oxygen consumption rates (JO_2)
866 of mitochondria isolated from whole kidney (D), and enriched proximal tubule (E), distal tubule
867 (F), and glomerular samples (G). H-K) ATP production rates (*J*ATP) of mitochondria isolated from
868 whole kidney (H), and enriched proximal tubule (I), distal tubule (J), and glomerular samples (K).
869 *P*: Pyruvate; *G*: Glutamate; *M*: Malate; *D*: ADP; *S*: Succinate.

870 **Figure 3**. Shematics outlining the foundational concept of the creatine kinase (CK) clamp assay.
871 The CK clamp assay works via modulating the ADP/ATP ratio under controlled bioenergetic
872 conditions using standard substrates and increasing phosphocreatine (PCr) concentration (A).
873 The use of PCr in the CK clamp allows for the controlled production of ATP under stable ADP
874 concentations, and further allows for the calculation of the Gibbs free energy of ATP synthesis
875 ($\Delta G'_{ATP}$), providing more detailed interrogation of bioenergetic properties of mitochondria (B). The
876 addition of PCr under these standard conditions will act as a bioenergetic "brake" on the
877 mitochondria, slowing the respiration rate as the [PCr] increases (C). Therefore, the controlled
878 bioenergetic state of the mitochondria can be used to estimate the conductance of the electron
879 transport chain via the slope of the relationship between oxygen consumption (JO_2) and $\Delta G'_{ATP}$
880 (D).

881 **Figure 4**. Results of the CK clamp assay on oxygen consumption rates (JO_2) in mitochondria
882 isolated from whole kidney cortex (A & B), and enriched proximal tubule (C & D), distal tubule (E
883 & F), and glomerular (G & H) samples. The conductance of the electron transport chain (ETC) in
884 each of our samples reveals differential ETC conductivity in the enriched samples (I), as well as
885 differing zero-load JO_2, which represents the conductivity of the ETC at minimal bioenergetic
886 resistance (i.e., $\Delta G'_{ATP} = 0$), shows differing bioenergetic profiles of the sieved fractions and the
887 isolated mitochondria, which are differentially impacted by adenine diet (J). *P*: Pyruvate; *G*:
888 Glutamate; *M*: Malate; *D*: ADP; *S*: Succinate; *Omy*: Oligomycin.

889 **Figure 5**. Results of the CK clamp assay on mitochondrial membrane potential ($\Delta\Psi'_{mt}$) in
890 mitochondria isolated from whole kidney cortex (A & B), and enriched proximal tubule (C & D),
891 distal tubule (E & F), and glomerular (G & H) samples. The coupling coefficient (I), or the slope of
892 the relationship between Gibbs free energy of ATP production and $\Delta\Psi_{mt}$, outlines the coupling
893 relationship between $\Delta\Psi'_{mt}$ and ATP production based on the chemiosmotic coupling theory
894 proposed by Peter Mitchell. The zero-load $\Delta\Psi'_{mt}$, which represents the coupling of $\Delta\Psi'_{mt}$ to ATP
895 production at minimal bioenergetic resistance (i.e., $\Delta G'_{ATP} = 0$) shows distinctive bioenergetic
896 properties of the isolated mitochondria and the enriched samples, which can also be influenced
897 by adenine feeding (J). *P*: Pyruvate; *G*: Glutamate; *M*: Malate; *D*: ADP; *S*: Succinate; *Omy*:
898 Oligomycin; *KCN*: Potassium cyanide.

899 **Figure 6**. A) Schematic outlining the sieving procedure in kidneys harvested from humans. B)
900 4X-microscopy images of the enriched tissue samples, indicating the yield and purity of the
901 enriched fractions obtained from this method. C) Initial pilot experiments showing that
902 mitochondrial respiration can be measured in enriched samples from humans. *P*: Pyruvate; *G*:
903 Glutamate; *M*: Malate; *D*: ADP; *S*: Succinate; *FCCP*: Carbonyl cyanide 4-
904 (trifluoromethoxy)phenylhydrazone.

905 **Figure S1.** qPCR of our fractions indicating that our samples were yielding enrichment of proximal
906 tubules (PT) at the 70 μm step, distal tubules (DT) at the 40 μm step, and glomeruli in the cell
907 culture dishes. *AQP2*: Aquaporin 2; *SGLT2*: Sodium-glucose cotransporter 2.

908 **Figure S2.** Body mass (A) and liver weights (B) at the time of euthanasia.

909 **Figure S3.** Quantification of hisological parameters obtained from the whole-slide images. Tubule
910 lumen area (A) and fibrotic area (B) were impacted by the adenine diet. Glomerular features, such
911 as corpuscle area and Bowman's Space (BS) were impacted by adenine diet, but not fibrotic area
912 or tuft area.

913 **Figure S4.** The relationship between oxygen consumption rates (JO_2) and mitochondrial
914 membrane potential ($\Delta\Psi'_{mt}$) in isolated mitochondria (A & B) and proximal tubules (C & D) shows
915 poor agreement, indicating that JO_2 alone is not a sufficient predictor of $\Delta\Psi'_{mt}$, likely due to
916 biological uncoupling mechanisms that are known to exist in mitochondrial membranes.

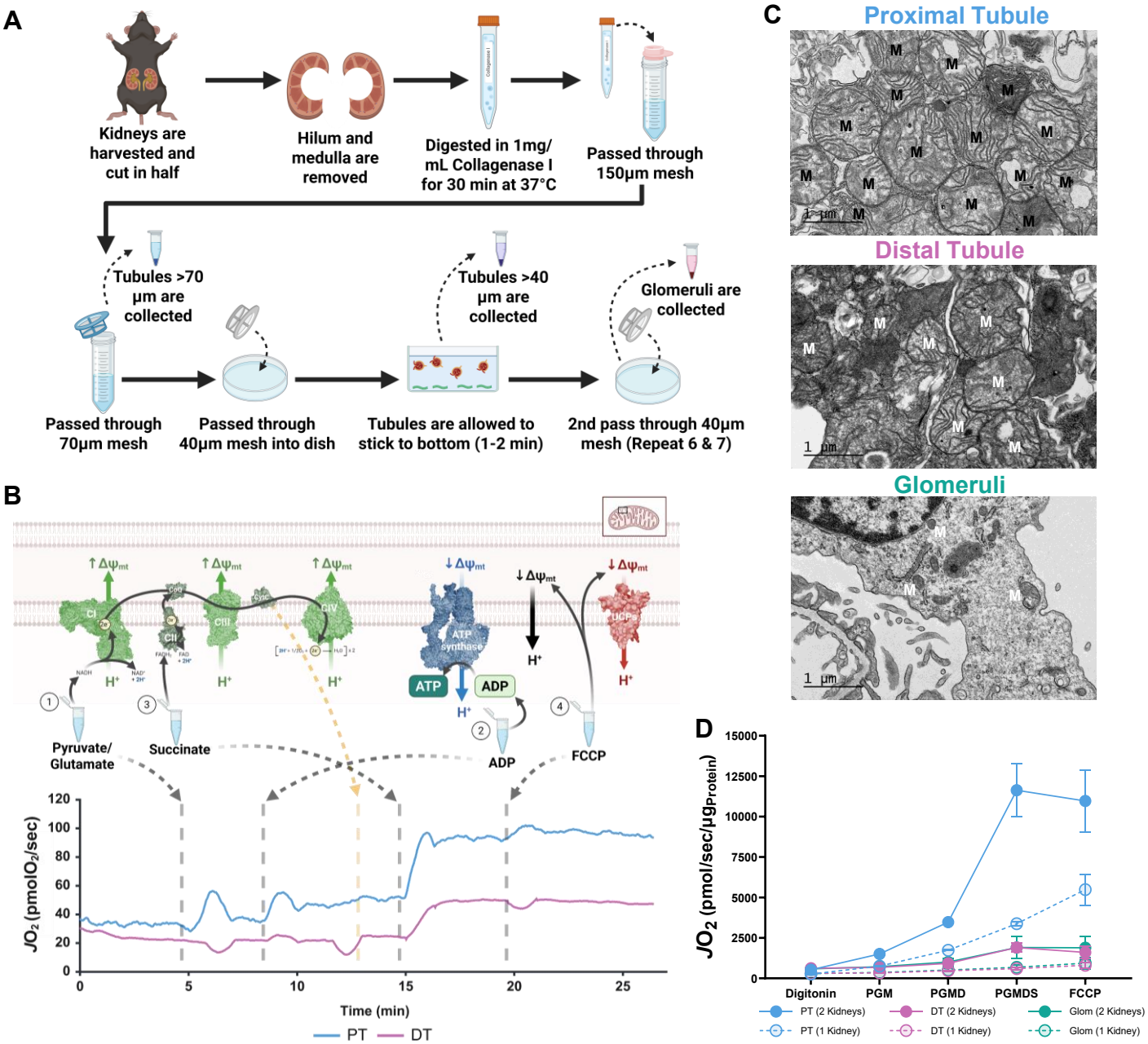
A
Kidneys are harvested and cut in half
Hilum and medulla are removed
Digested in 1mg/ mL Collagenase I for 30 min at 37°C
Passed through 150µm mesh
Tubules >70 µm are collected
Passed through 70µm mesh
Passed through 40µm mesh into dish
Tubules >40 µm are collected
Tubules are allowed to stick to bottom (1-2 min)
Glomeruli are collected
2nd pass through 40µm mesh (Repeat 6 & 7)
B
Pyruvate/ Glutamate
Succinate
ADP
FCCP
ATP
ADP
JO2 (pmolO2/sec)
Time (min)
PT
DT
C
Proximal Tubule
Distal Tubule
Glomeruli
D
JO2 (pmol/sec/µgProtein)
Digitonin
PGM
PGMD
PGMDS
FCCP
PT (2 Kidneys)
DT (2 Kidneys)
Glom (2 Kidneys)
PT (1 Kidney)
DT (1 Kidney)
Glom (1 Kidney)

Figure 1

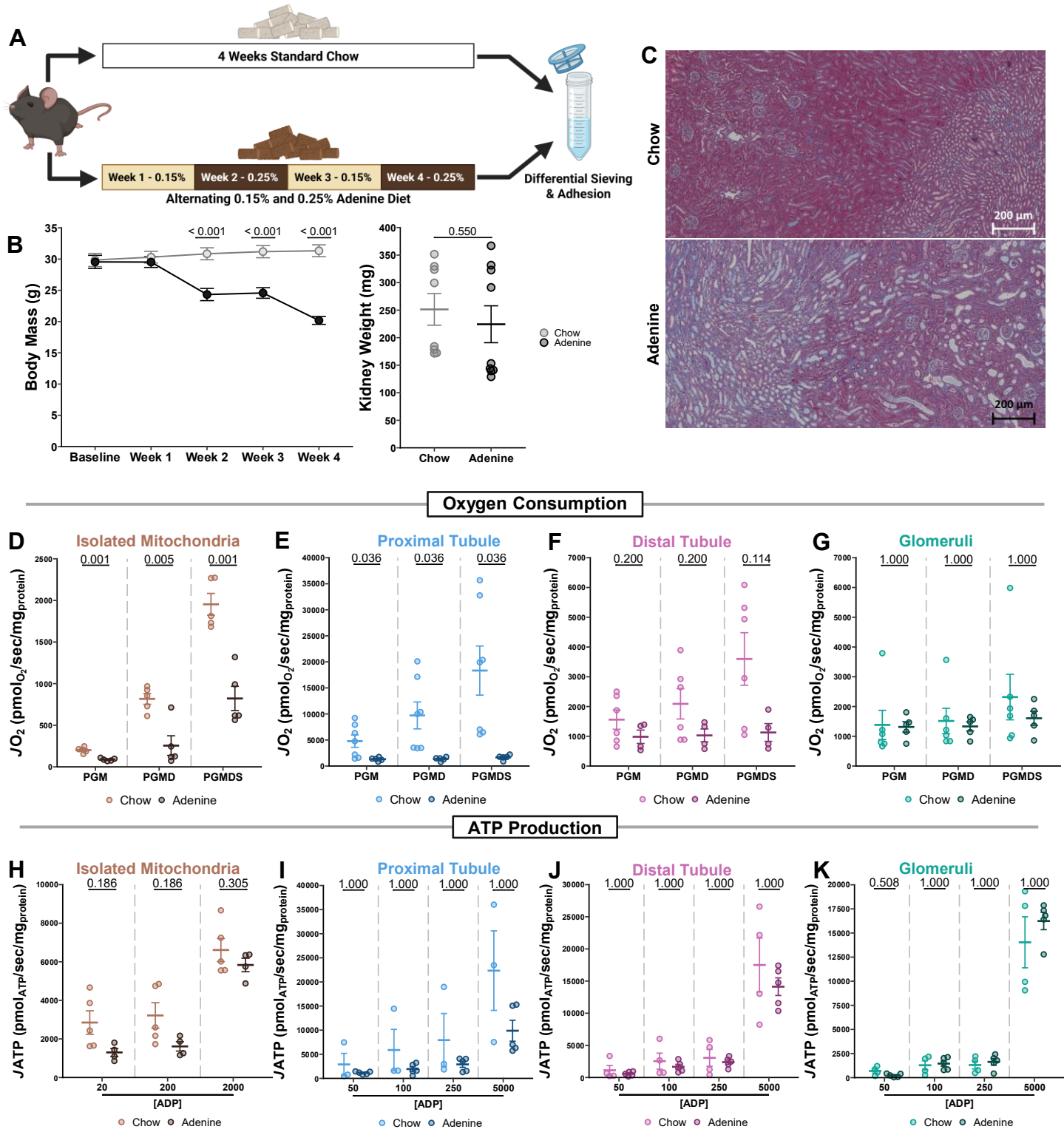
A
4 Weeks Standard Chow
Week 1 - 0.15%
Week 2 - 0.25%
Week 3 - 0.15%
Week 4 - 0.25%
Alternating 0.15% and 0.25% Adenine Diet
Differential Sieving & Adhesion
B
Body Mass (g)
< 0.001
< 0.001
< 0.001
Baseline
Week 1
Week 2
Week 3
Week 4
Kidney Weight (mg)
0.550
Chow
Adenine
C
Chow
Adenine
200 µm
200 µm
Oxygen Consumption
D
Isolated Mitochondria
0.001
0.005
0.001
E
Proximal Tubule
0.036
0.036
0.036
F
Distal Tubule
0.200
0.200
0.114
G
Glomeruli
1.000
1.000
1.000
JO2 (pmolO2/sec/mgprotein)
PGM
PGMD
PGMDS
Chow
Adenine
ATP Production
H
Isolated Mitochondria
0.186
0.186
0.305
I
Proximal Tubule
1.000
1.000
1.000
1.000
J
Distal Tubule
1.000
1.000
1.000
1.000
K
Glomeruli
0.508
1.000
1.000
1.000
JATP (pmolATP/sec/mgprotein)
[ADP]
20
200
2000
50
100
250
5000
Chow
Adenine

Figure 2

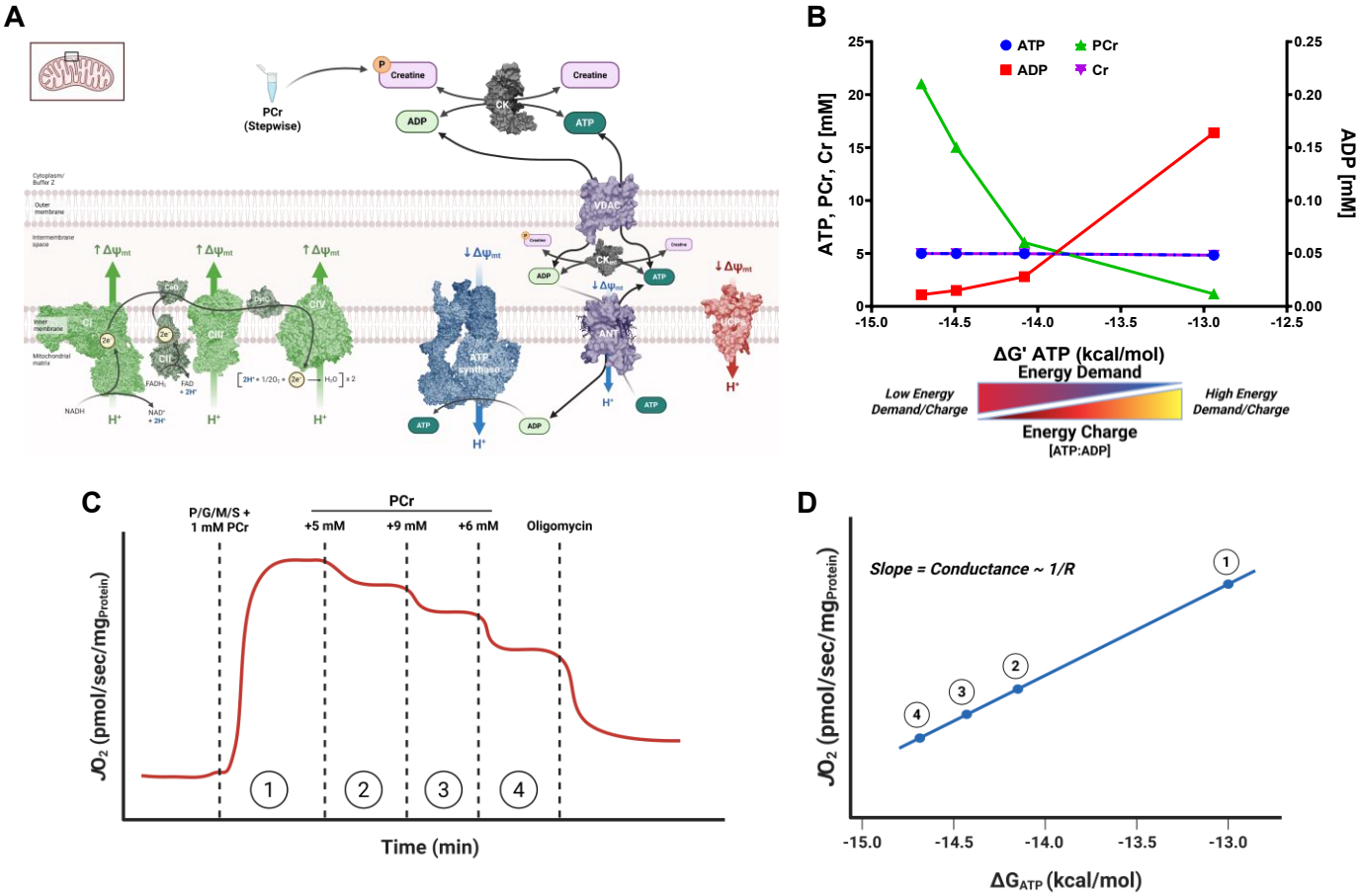
A
PCr
(Stepwise)
Creatine
Creatine
CK
ADP
ATP
VDAC
CK
ADP
ATP
ANT
ATP synthase
ADP
ATP
H+
B
ATP
PCr
ADP
Cr
ATP, PCr, Cr [mM]
ADP [mM]
ΔG' ATP (kcal/mol)
Energy Demand
Low Energy Demand/Charge
High Energy Demand/Charge
Energy Charge
[ATP:ADP]
C
P/G/M/S +
1 mM PCr
PCr
+5 mM
+9 mM
+6 mM
Oligomycin
JO2 (pmol/sec/mgProtein)
Time (min)
D
Slope = Conductance ~ 1/R
JO2 (pmol/sec/mgProtein)
ΔGATP (kcal/mol)

Figure 3

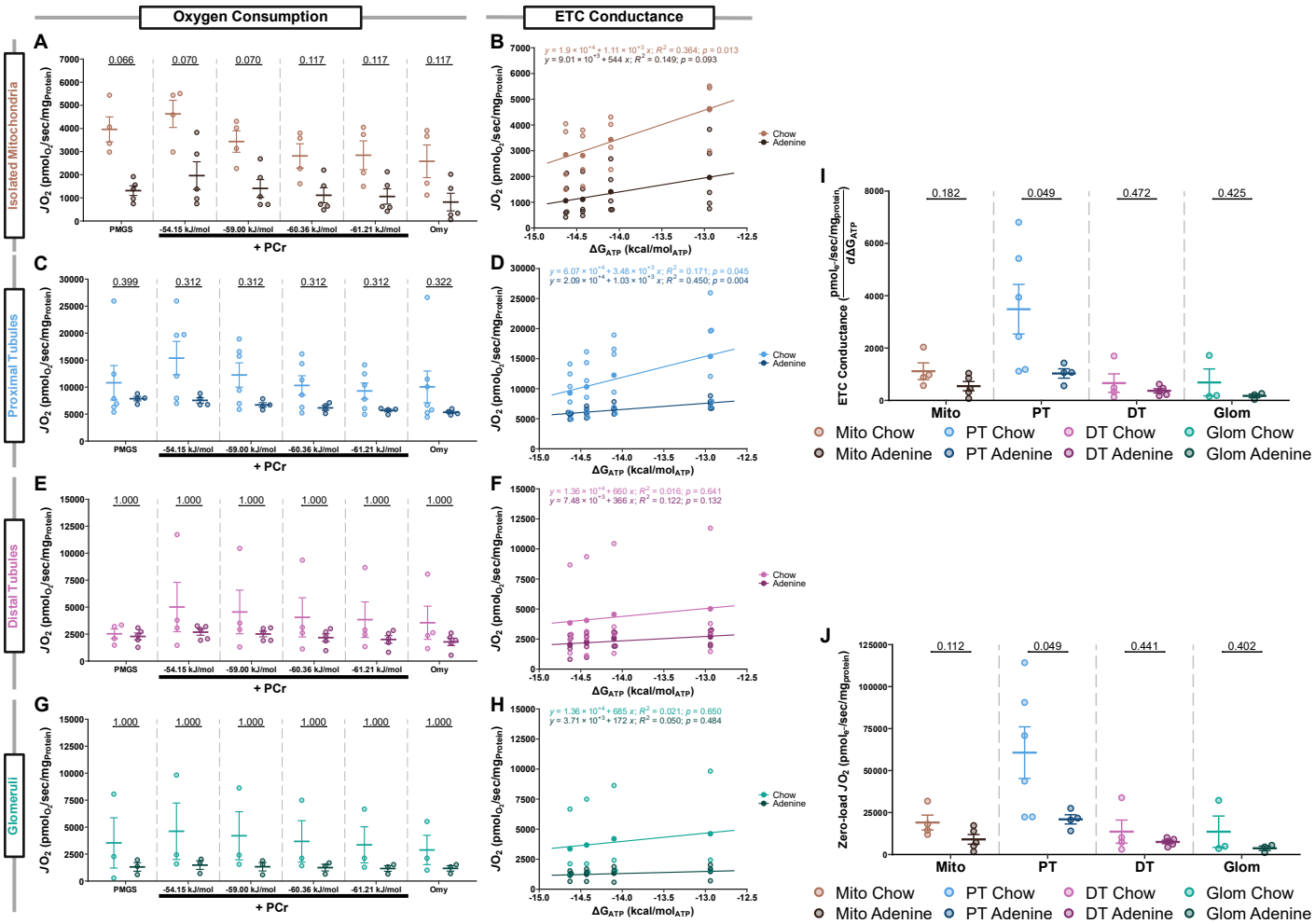
Oxygen Consumption
ETC Conductance
Isolated Mitochondria
Proximal Tubules
Distal Tubules
Glomeruli
A
B
C
D
E
F
G
H
I
J
PMGS
-54.15 kJ/mol
-59.00 kJ/mol
-60.36 kJ/mol
-61.21 kJ/mol
Omy
+ PCr
Chow
Adenine
Mito
PT
DT
Glom
Mito Chow
Mito Adenine
PT Chow
PT Adenine
DT Chow
DT Adenine
Glom Chow
Glom Adenine

Figure 4

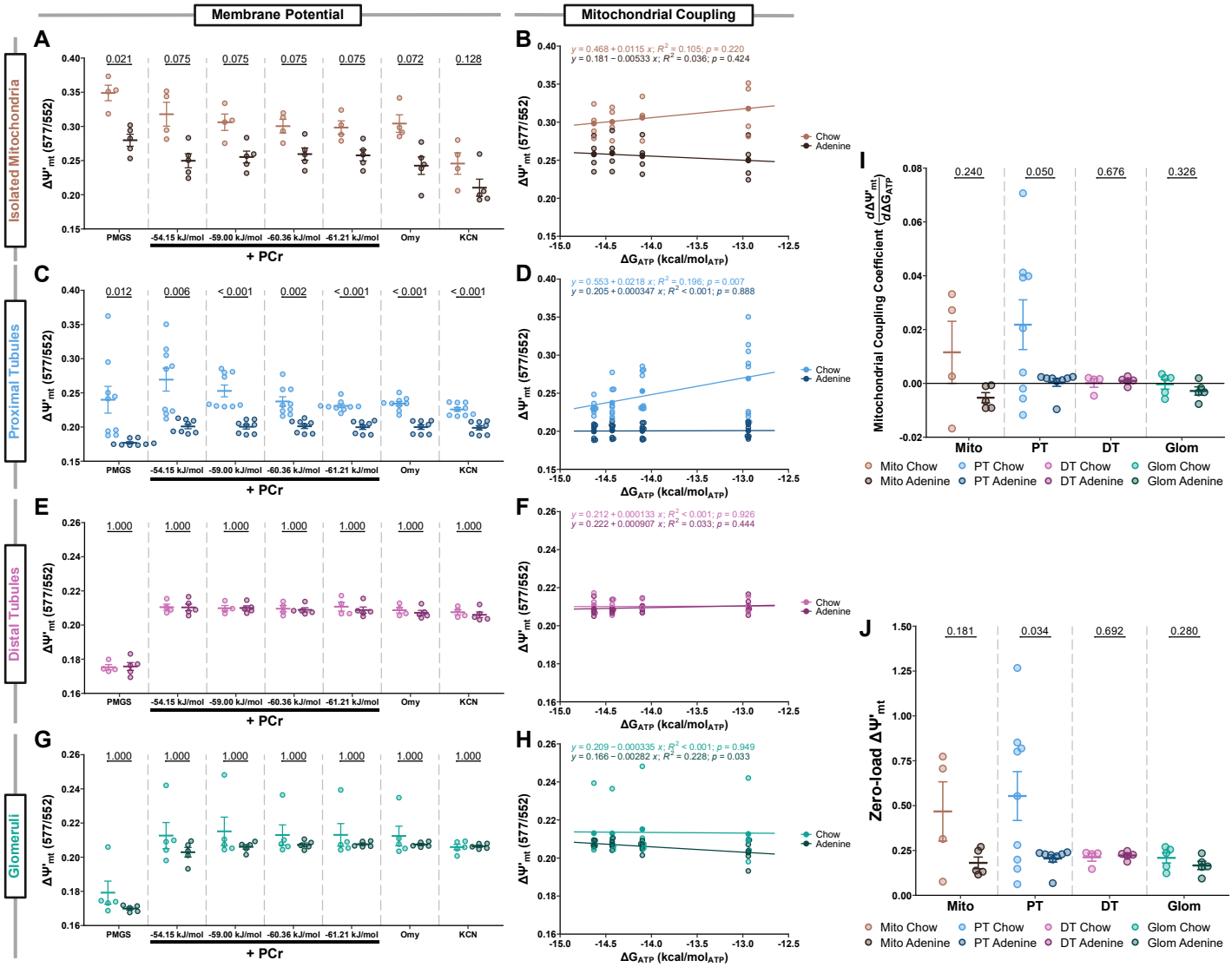
Membrane Potential
Mitochondrial Coupling
Isolated Mitochondria
Proximal Tubules
Distal Tubules
Glomeruli
A
B
C
D
E
F
G
H
I
J
ΔΨ'mt (577/552)
PMGS
-54.15 kJ/mol
-59.00 kJ/mol
-60.36 kJ/mol
-61.21 kJ/mol
Omy
KCN
+ PCr
0.021
0.075
0.075
0.075
0.075
0.072
0.128
0.012
0.006
< 0.001
0.002
< 0.001
< 0.001
< 0.001
1.000
y = 0.468 + 0.0115 x; R2 = 0.105; p = 0.220
y = 0.181 − 0.00533 x; R2 = 0.036; p = 0.424
y = 0.553 + 0.0218 x; R2 = 0.196; p = 0.007
y = 0.205 + 0.000347 x; R2 < 0.001; p = 0.888
y = 0.212 + 0.000133 x; R2 < 0.001; p = 0.926
y = 0.222 + 0.000907 x; R2 = 0.033; p = 0.444
y = 0.209 − 0.000335 x; R2 < 0.001; p = 0.949
y = 0.166 − 0.00282 x; R2 = 0.228; p = 0.033
Chow
Adenine
ΔGATP (kcal/molATP)
Mitochondrial Coupling Coefficient d(ΔΨ'mt)/d(ΔGATP)
0.240
0.050
0.676
0.326
Mito
PT
DT
Glom
Zero-load ΔΨ'mt
0.181
0.034
0.692
0.280
Mito Chow
Mito Adenine
PT Chow
PT Adenine
DT Chow
DT Adenine
Glom Chow
Glom Adenine

Figure 5

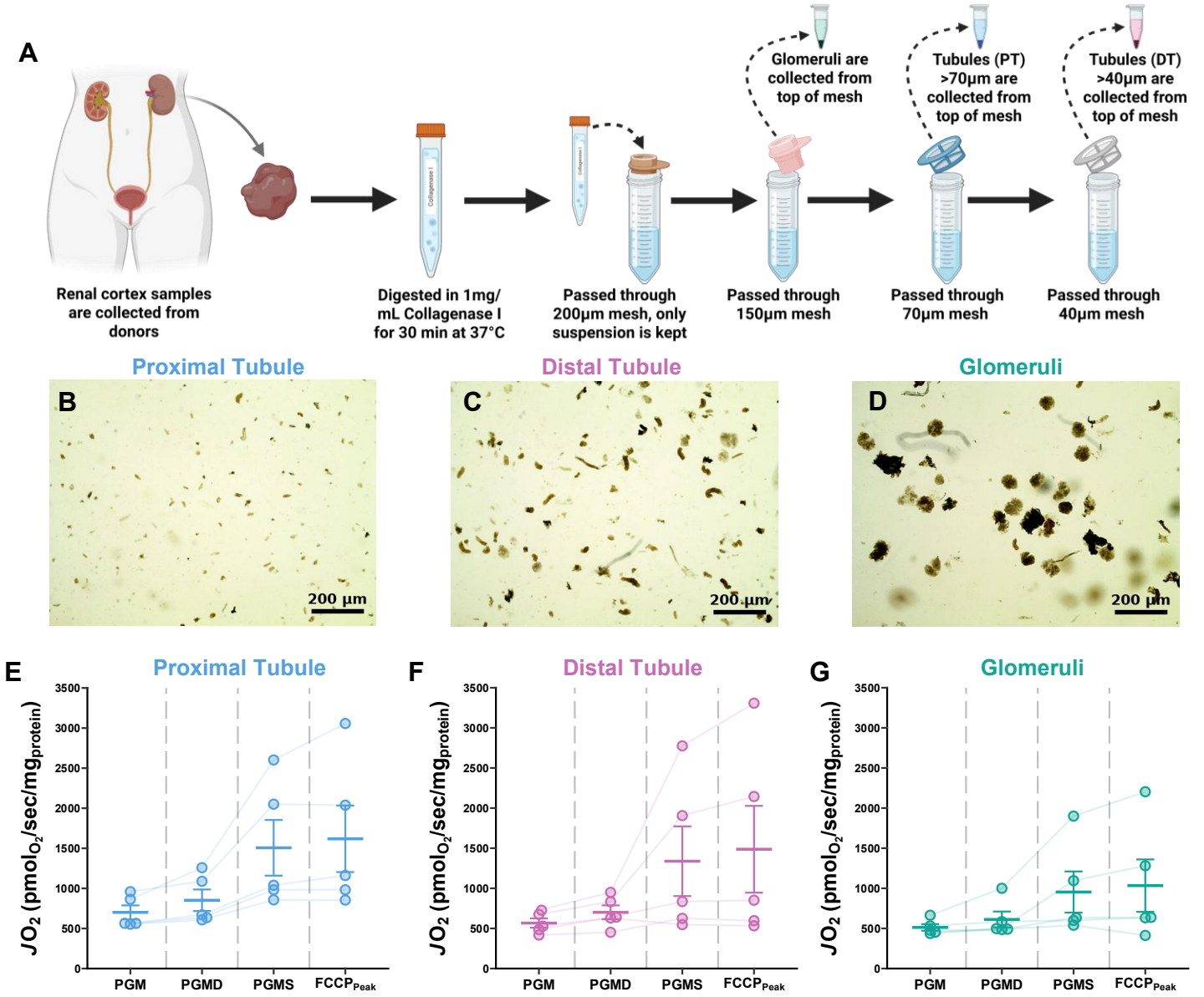
A
Renal cortex samples are collected from donors
Digested in 1mg/ mL Collagenase I for 30 min at 37°C
Passed through 200µm mesh, only suspension is kept
Glomeruli are collected from top of mesh
Passed through 150µm mesh
Tubules (PT) >70µm are collected from top of mesh
Passed through 70µm mesh
Tubules (DT) >40µm are collected from top of mesh
Passed through 40µm mesh
Proximal Tubule
B
200 µm
Distal Tubule
C
200 µm
Glomeruli
D
200 µm
E
Proximal Tubule
F
Distal Tubule
G
Glomeruli
JO2 (pmolO2/sec/mgprotein)
3500
3000
2500
2000
1500
1000
500
0
PGM
PGMD
PGMS
FCCPPeak

Figure 6

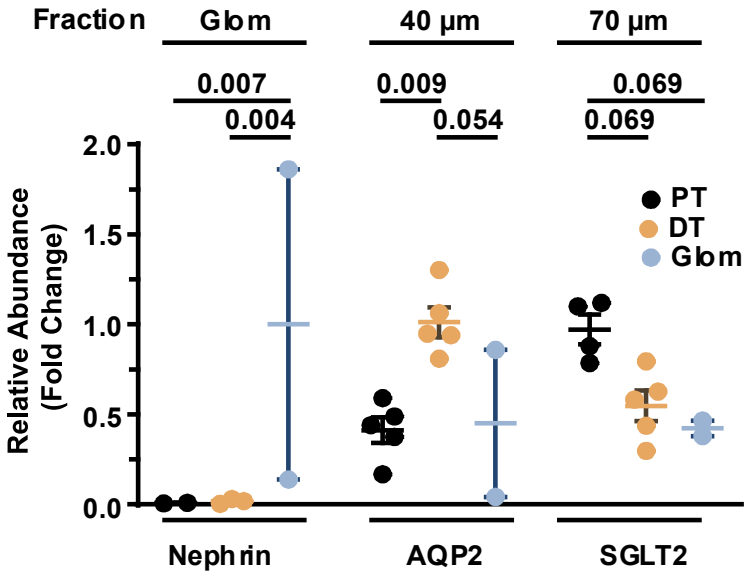
Fraction
Glom
40 µm
70 µm
0.007
0.004
0.009
0.054
0.069
0.069
Relative Abundance
(Fold Change)
2.0
1.5
1.0
0.5
0.0
PT
DT
Glom
Nephrin
AQP2
SGLT2

Figure S1

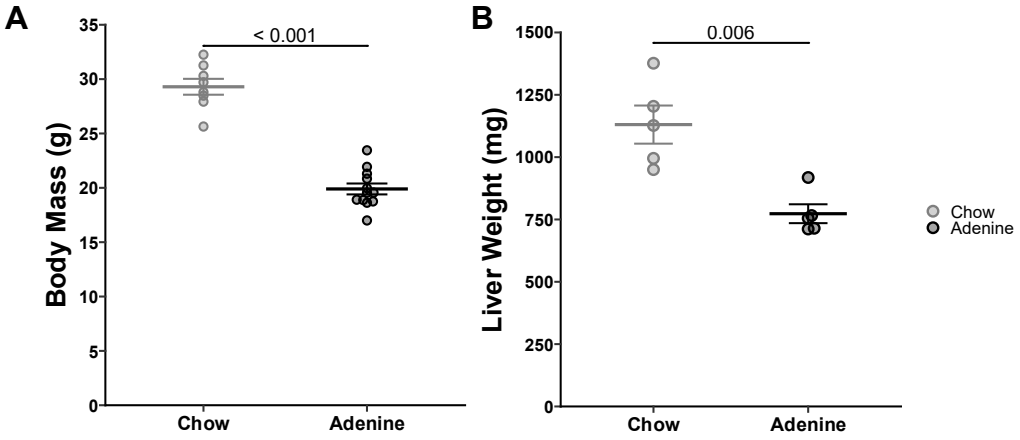
A
< 0.001
Body Mass (g)
35
30
25
20
15
10
5
0
Chow
Adenine
B
0.006
Liver Weight (mg)
1500
1250
1000
750
500
250
0
Chow
Adenine
Chow
Adenine

Figure S2

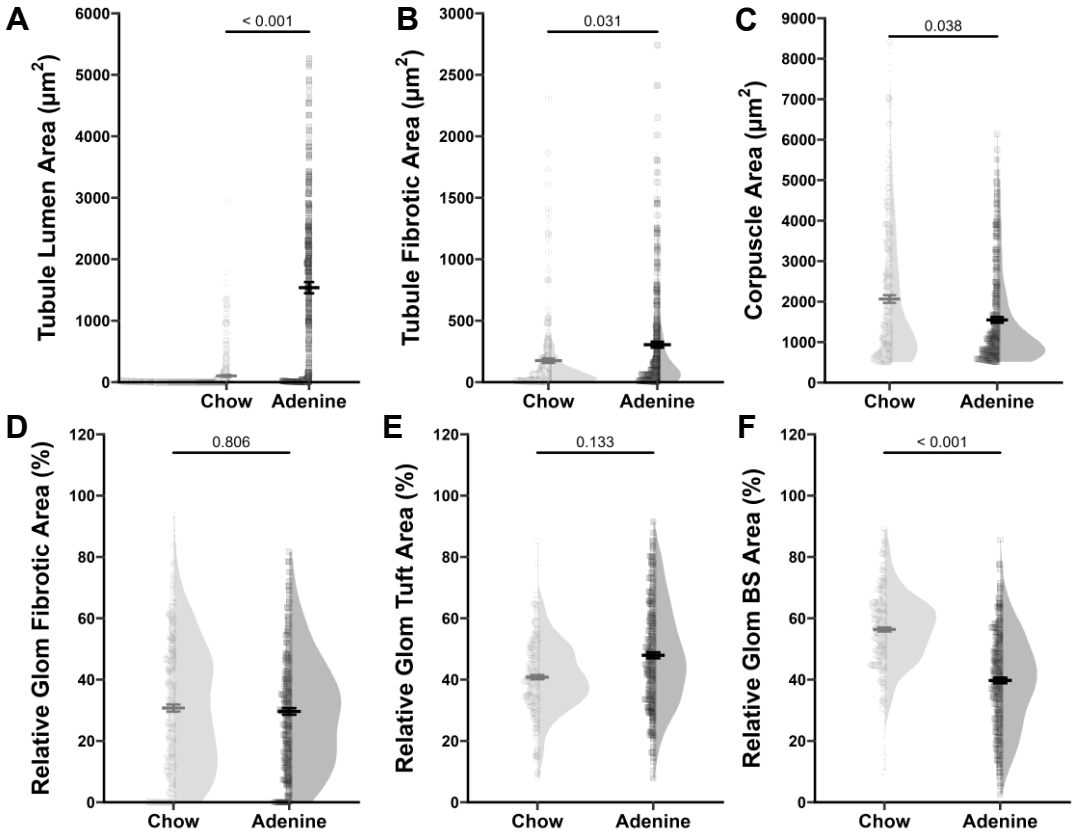
A
Tubule Lumen Area (μm²)
< 0.001
Chow
Adenine
B
Tubule Fibrotic Area (μm²)
0.031
Chow
Adenine
C
Corpuscle Area (μm²)
0.038
Chow
Adenine
D
Relative Glom Fibrotic Area (%)
0.806
Chow
Adenine
E
Relative Glom Tuft Area (%)
0.133
Chow
Adenine
F
Relative Glom BS Area (%)
< 0.001
Chow
Adenine

Figure S3

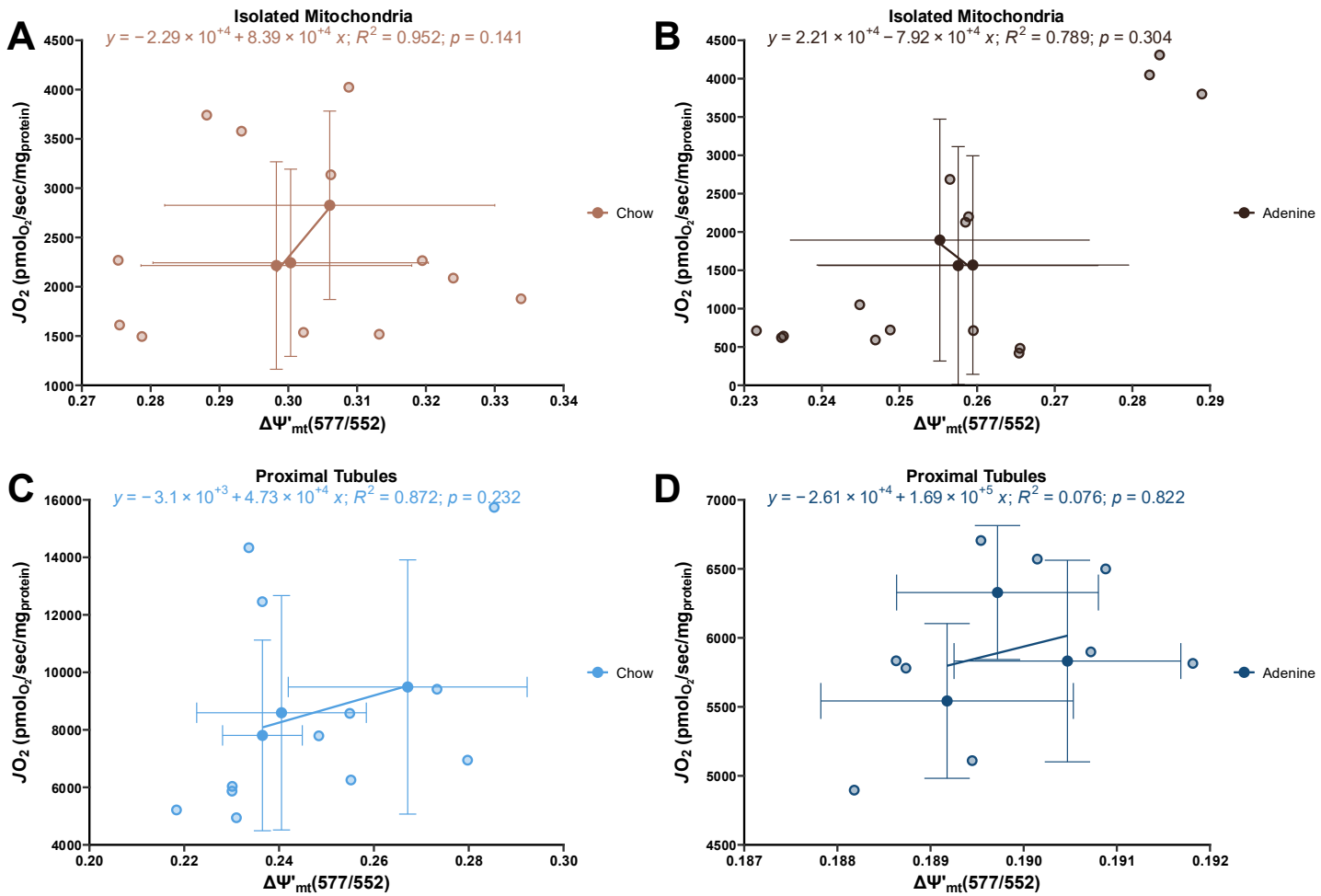
A
Isolated Mitochondria
y = −2.29 × 10+4 + 8.39 × 10+4 x; R2 = 0.952; p = 0.141
JO2 (pmolO2/sec/mgprotein)
ΔΨ'mt(577/552)
Chow
B
Isolated Mitochondria
y = 2.21 × 10+4 − 7.92 × 10+4 x; R2 = 0.789; p = 0.304
JO2 (pmolO2/sec/mgprotein)
ΔΨ'mt(577/552)
Adenine
C
Proximal Tubules
y = −3.1 × 10+3 + 4.73 × 10+4 x; R2 = 0.872; p = 0.232
JO2 (pmolO2/sec/mgprotein)
ΔΨ'mt(577/552)
Chow
D
Proximal Tubules
y = −2.61 × 10+4 + 1.69 × 10+5 x; R2 = 0.076; p = 0.822
JO2 (pmolO2/sec/mgprotein)
ΔΨ'mt(577/552)
Adenine

Figure S4